Smith-Magenis syndrome protein RAI1 regulates body weight homeostasis through hypothalamic BDNF-producing neurons and neurotrophin downstream signalling

Sehrish Javed[1,2], Ya-Ting Chang[1,2], Yoobin Cho[1,2], Yu-Ju Lee[1,2], Hao-Cheng Chang[1,2], Minza Haque[1,2], Yu Cheng Lin[1,2], Wei-Hsiang Huang[1,2,*]

Affiliations:

[1]Department of Neurology and Neurosurgery, Centre for Research in Neuroscience, McGill University, Montréal, QC H3G 1A3, Canada

[2]Brain Repair and Integrative Neuroscience Program, The Research Institute of the McGill University Health Centre, Montréal, QC H3G 1A3, Canada

*Corresponding author. Email: wei-hsiang.huang@mcgill.ca

Abstract

Retinoic acid-induced 1 (*RAI1*) haploinsufficiency causes Smith-Magenis syndrome (SMS), a genetic disorder with symptoms including hyperphagia, hyperlipidemia, severe obesity, and autism phenotypes. RAI1 is a transcriptional regulator with a pan-neural expression pattern and hundreds of downstream targets. The mechanisms linking neural *Rai1* to body weight regulation remain unclear. Here we find that hypothalamic brain-derived neurotrophic factor (BDNF) and its downstream signalling are disrupted in SMS ($Rai1^{+/-}$) mice. Selective *Rai1* loss from all BDNF-producing cells or from BDNF-producing neurons in the paraventricular nucleus of the hypothalamus (PVH) induced obesity in mice. Electrophysiological recordings revealed that *Rai1* ablation decreased the intrinsic excitability of PVH^{BDNF} neurons. Chronic treatment of SMS mice with LM22A-4 engages neurotrophin downstream signalling and delayed obesity onset. This treatment also partially rescued disrupted lipid profiles, insulin intolerance, and stereotypical repetitive behaviour in SMS mice. These data argue that RAI1 regulates body weight and metabolic function through hypothalamic BDNF-producing neurons and that targeting neurotrophin downstream signalling might improve associated SMS phenotypes.

Introduction

Obesity is an increasing global concern: 20% of the world's adult population is expected to become obese by 2025 if current trends persist (Collaboration, 2017). However, the complex environmental, behavioural, and genetic contributions to obesity make this a complex condition to model and address. Monogenic obesity disorders provide a consistent system where the pathophysiology, genetic predisposition, and neurobiology underlying phenotypes can potentially provide insights that translate to polygenic obesity (Loos & Yeo, 2022).

One such monogenic disorder is Smith-Magenis syndrome (SMS; OMIM #182290) (Smith *et al*, 1986), a neurogenetic condition frequently associated with obesity. 80% of SMS cases are caused by interstitial deletions of the 17p11.2 chromosomal region containing a dosage-sensitive gene, *retinoic acid-induced 1* (*RAI1*) (Slager *et al*, 2003). Most SMS patients are overweight (40% > 95th percentile weight, 80% > 85th percentile weight) and exhibit over-eating tendencies by adolescence (Alaimo *et al*, 2015; Burns *et al*, 2010; Gandhi *et al*, 2022). 20% of SMS patients do not have 17p11.2 deletions but instead carry *RAI1* point mutations that are still frequently associated with obesity (Boot *et al*, 2021; Edelman *et al*, 2007). These clinical data indicate that RAI is critical for body weight regulation.

The human RAI1 protein shares >80% sequence identity with the mouse RAI1 protein, allowing us to study RAI1 function *in vivo* (Huang *et al*, 2016; Javed *et al*, 2020). We previously found that *Rai1* encodes a transcriptional regulator that binds to the promoter or enhancer regions of its target genes, most of which are involved in neurodevelopment and synaptic transmission (Huang *et al.*, 2016). SMS (*Rai1*$^{+/-}$) mice exhibit obesity associated with hyperphagia and increased adiposity (Burns *et al.*, 2010; Huang *et al.*, 2016). Interestingly, RAI1 may have a sexually

60 dimorphic function, as female SMS mice exhibit more pronounced obesity than males (Burns *et*
61 *al.*, 2010; Huang *et al.*, 2016).

62 Using a homozygous *Rai1* conditional knockout (*Rai1*-cKO) mice, we found that *Rai1* deletion
63 in either subcortical excitatory neurons (vGlut2$^+$) or single-minded homolog 1 (Sim1$^+$) neurons
64 induced obesity in mice (Huang *et al.*, 2016). Sim1$^+$ neurons reside in several brain regions
65 including the nucleus of the lateral olfactory tract, the supraoptic nucleus, the medial amygdala,
66 and the paraventricular nucleus of the hypothalamus (PVH), a region that is critical for body
67 weight regulation (Balthasar *et al*, 2005). Sim1$^+$ neurons in the PVH are composed of several
68 molecularly defined cell types, including those that express oxytocin, vasopressin, corticotropin-
69 releasing hormone, somatostatin, melanocortin-4-receptor (MC4R), growth hormone-releasing
70 hormone (GHRH), or brain-derived neurotrophic factor (BDNF) (An *et al*, 2015). Deleting *Bdnf*
71 from the PVH results in obesity due to increased food intake, reduced energy expenditure, and
72 reduced locomotion (An *et al.*, 2015). While PVH neuronal activity is reduced during feeding
73 (Xu *et al*, 2019), activation of PVH^{BDNF} neurons results in weight loss (Wu & Xu, 2022). We
74 recently found that RAI1 promotes *Bdnf* expression in the hypothalamus throughout life (Javed
75 *et al*, 2021). We hypothesized that RAI11 may be connected to BDNF-producing neurons in
76 PVH, explaining how a neural transcription factor regulates body weight homeostasis.

77 BDNF regulates energy metabolism by binding to its cognate receptor tropomyosin receptor
78 kinase B (TRKB) (An *et al.*, 2015) and may thus provide a potential therapeutic target for SMS.
79 However, the link between *RAI1, BDNF*, and SMS symptoms is unclear. Patients carrying
80 monogenic mutations in either *BDNF* (Gray *et al*, 2006) or *NTRK2* (encoding TRKB) (Yeo *et al*,
81 2004) experience severe hyperphagic obesity. Moreover, obesity and associated metabolic
82 dysfunctions such as impaired glucose and insulin sensitivity are correlated with impaired PI3K-

83 AKT pathway, a TRKB downstream target (Su *et al*, 2021). Given that (1) *Bdnf* overexpression
84 during early embryonic development or (2) targeting *Bdnf* overexpression to the PVH of
85 adolescent SMS (*Rai1*$^{+/-}$) mice protected them from weight gain and metabolic defects (Javed *et*
86 *al.*, 2021), and that (3) a point mutation in *RAI1* disrupts its ability to transcriptionally enhance
87 *BDNF* expression *in vitro* (Abad *et al*, 2018), pharmacological targeting of neurotrophin
88 downstream signalling is an attractive and yet unexplored therapeutic avenue for SMS.

89 Building on our previous discoveries, here we examine the neurobiological functions of RAI1 in
90 BDNF-producing neurons, specifically those that reside in the PVH. Importantly, we evaluated
91 the involvement of the BDNF-TRKB pathways in SMS pathogenesis using a small molecule
92 drug (LM22A-4) to enhance neurotrophin downstream signalling. Our work indicates that
93 PVH^{BDNF} neurons depend on RAI1 to maintain normal neuronal activity and regulate body
94 weight homeostasis, and dysfunction of BDNF downstream signalling contributes to obesity
95 associated with SMS mice.

96

97 **Results**

98 ***Rai1* deficiency dysregulates specific downstream targets of neurotrophin in the mouse**
99 **hypothalamus**

100 Multiple lines of evidence indicated that SMS mice show decreased *Bdnf* mRNA expression in
101 the hypothalamus (Burns *et al.*, 2010; Huang *et al.*, 2016; Javed *et al.*, 2021). To determine if
102 BDNF protein levels were consequently altered in the hypothalamus, we performed an enzyme-
103 linked immunosorbent assay (ELISA) and found that BDNF protein levels were significantly
104 reduced in 7-week-old pre-symptomatic SMS mice relative to controls (**Fig 1A**). To quantify if
105 molecular pathways associated with BDNF downstream signalling were altered, we subjected
106 hypothalamic tissue lysates from 7-week-old pre-obese SMS and control (Ctrl) mice to reverse
107 phase protein array (RPPA) (**Fig 1B**). Control and SMS samples are clustered separately in the
108 principal component analysis (**Fig 1C**).

109 Hierarchical clustering analysis indicated that most differentially expressed phosphorylated
110 proteins (**Fig 1D**) and total proteins (**Figure 1—figure supplement 1**) were downregulated in
111 SMS mice. We mapped total proteins, as well as phospho-proteins, that were differentially
112 expressed in Ctrl and SMS samples onto the interconnected biological network and identified a
113 subset of connected nodes downregulated in SMS (FDR < 10e-5) belong to the neurotrophin,
114 PI3K-AKT, and mTOR signalling cascades (**Fig 1E**). These molecules are known to play a
115 critical role in regulating body weight homeostasis and can be activated by BDNF either directly
116 (neurotrophin pathway) or indirectly (PI3K-AKT and mTOR pathways) (Cota *et al*, 2006;
117 Schultze *et al*, 2012). The expression levels of PIK3CA, a common node in these pathways, were
118 significantly reduced in the SMS mice compared to controls (**Fig 1F**). Moreover, the expression
119 levels of phosphorylated NF-κB (nuclear factor-kappa B), a downstream target of the

120 neurotrophin pathway, were significantly reduced in the SMS group (**Fig 1G**). Together, these
121 results suggest that *Rai1* loss impairs specific pathways, including neurotrophin signalling, and
122 indicate that dysfunction of BDNF-producing cells could contribute to SMS pathogenesis.

123

124 **BDNF-producing cells depend on RAI1 to regulate body weight homeostasis**

125 To target BDNF-producing cells, we used a *Bdnf*$^{Cre/+}$ mouse line that carries a viral 2A
126 oligopeptide and Cre recombinase immediately upstream of *Bdnf*'s endogenous STOP codon
127 (Tan *et al*, 2016). We crossed the *Bdnf*$^{Cre/+}$ mice with tdTomato-Ai9 reporter mice and found that
128 Ai9 signals faithfully reflected endogenous BDNF protein expression in the PVH (**Figure 2—**
129 **figure supplement 1A-E**). We also found that RAI1 is expressed in PVH^{BDNF} cells that are
130 distinct from larger magnocellular cells, such as the PVH oxytocin neurons (**Figure 2—figure**
131 **supplement 2A-I**). Specifically, 55% of PVH^{BDNF} neurons express RAI1, whereas only 2% of
132 PVH^{Oxytocin} neurons express RAI1 (**Figure 2—figure supplement 2I**). These data suggest that
133 RAI1 is enriched in BDNF-producing neurons in the mouse PVH.

134 To determine if BDNF-producing cells depend on RAI1 to regulate body weight, we deleted one
135 or both copies of *Rai1* using the *Bdnf*$^{Cre/+}$ and the conditional *Rai1*$^{fl/fl}$ mice (Huang *et al.*, 2016)
136 (**Fig 2A, Figure 2—figure supplement 3A**). Conditional knockout mice (cKO: *Bdnf*$^{Cre/+}$;
137 *Rai1*$^{fl/fl}$) showed a significant reduction in Rai1 expression in PVH^{BDNF} neurons compared to
138 controls (**Fig 2B-C**, **Figure 2—figure supplement 3B)**. The total number of BDNF-producing
139 cells in the PVH remained similar in Ctrl and cKO mice (**Figure 2—figure supplement 3C**),
140 indicating that RAI1 loss did not affect PVH neurogenesis or survival.

141 We monitored body weight weekly and found that male and female cKO mice showed a
142 significant increase in body weight beginning at 15 weeks of age compared to controls (Ctrl:
143 *Bdnf*$^{Cre/+}$) (**Fig 2D**, **Figure 2—figure supplement 4A**). However, conditional *Rai1* heterozygous
144 mice (*Bdnf*$^{Cre/+}$; *Rai1*$^{fl/+}$) did not show a pathological increase in body weight (**Figure 2—figure**
145 **supplement 3D**, **Figure 2—figure supplement 4B**), suggesting that non-BDNF-producing cells
146 also contribute to SMS pathogenesis. EcoMRI found that 26-week-old cKO male and female
147 mice showed increased fat mass but not lean mass (**Fig 2E**, **Figure 2—figure supplement 4C**).
148 Further dissection of fat tissues from different organs showed an increased mass of subcutaneous
149 inguinal (S.C. Ing.) fat in cKO mice of both sexes and an increased mass of epididymal adipose
150 tissues (eWAT) in female cKOs (**Fig 2F**, **Figure 2—figure supplement 4D**).

151 In contrast, the total mass of brown adipose tissue (BAT) remained unchanged between groups
152 (**Fig 2F**, **Figure 2—figure supplement 4D**). In both male and female cKO mice, we found
153 hypertrophic eWAT adipocytes (**Fig 2G**, **Figure 2—figure supplement 4E**) and elevated blood
154 leptin levels (**Fig 2H**, **Figure 2—figure supplement 4F**). However, there was no significant
155 alteration in blood lipids such as triglycerides (TG), high-density lipoprotein (HDL), low-density
156 lipoproteins (LDL), and very low-density lipoprotein (VLDL) in either male or female cKO mice
157 (**Figure 2—figure supplement 3E-G**, **Figure 2—figure supplement 4G-I)**. These data suggest
158 that obesity caused by ablating *Rai1* from BDNF-producing cells is associated with increased fat
159 mass, fat deposition, and leptin levels.

160 Obesity could result from increased food intake, reduced energy expenditure, or both. Similar to
161 SMS mice, male and female cKO mice did not have defects in respiratory exchange rates when
162 measured by indirect calorimetry (**Figure 2—figure supplement 3H**, **Figure 2—figure**
163 **supplement 4J**). Interestingly, cKO mice showed sex-specific differences in energy expenditure.

164 During the dark phase, female cKO mice showed reduced energy expenditure (Fig 2I) and
165 decreased total locomotor activity (**Fig 2J**). In contrast, total food intake remained unchanged
166 (**Fig 2K**). Male cKO mice became hyperphagic (**Figure 2—figure supplement 4K**), showed
167 increased energy expenditure during the dark phase (**Figure 2—figure supplement 4L**), and
168 exhibited normal locomotor activity when compared to controls (**Figure 2—figure supplement**
169 **4M**). These results suggest that obesity in male cKO mice is attributable to overeating despite
170 increased energy expenditure.

171 To determine if *Rai1* loss from BDNF-producing cells impacts metabolic function, a glucose
172 tolerance test (GTT) was performed. Interestingly, cKO mice of both sexes showed normal blood
173 glucose levels right before the test but became hyperglycemic 20 minutes (female cKO) and 45
174 minutes (male cKO) after glucose administration (**Fig 2L**, **Figure 2—figure supplement 4N**).
175 This change was accompanied by a significantly higher area under the curve (AUC) for both
176 groups (**Figure 2—figure supplement 3I**, **Figure 2—figure supplement 4O**). While the male
177 cKO mice remained hyperglycemic throughout the GTT (**Figure 2—figure supplement 4N**), the
178 glucose levels in female cKO mice returned to normal towards the end (**Fig 2L**). We also found
179 increased blood insulin levels during the GTT in both sexes (**Figure 2—figure supplement 3J**,
180 **Figure 2—figure supplement 4P**). In the insulin tolerance test (ITT), female cKO mice showed
181 moderately elevated glucose levels 20 minutes into the test (**Figure 2—figure supplement 3K**).
182 By contrast, male cKO mice showed considerably higher glucose levels than controls in the ITT
183 (~6.5 ng/ml for cKO and ~2.0ng/ml for Ctrl) during the 60- to 120-minute intervals (**Figure 2—**
184 **figure supplement 4Q**). These experiments demonstrate that BDNF-producing cells depend on
185 RAI1 to regulate body weight, adiposity, glucose and insulin tolerance in mice.

186

187 ***Rai1* deletion reduces PVH^{BDNF} neuronal excitability**

188 BDNF-producing neurons are widely distributed in the hypothalamus, being found in the
189 dorsomedial hypothalamus (Unger *et al*, 2007), ventromedial hypothalamus (Xu *et al*, 2003), and
190 PVH (An *et al.*, 2015). To understand how *Rai1* loss affects intrinsic neuronal excitability and
191 synaptic transmission of PVH^{BDNF} neurons that underlie energy homeostasis (An *et al.*, 2015),
192 we fluorescently labelled them with Cre-dependent tdTomato (**Fig. 3A**). We found that a
193 hyperpolarized step followed by increasing the holding voltage at resting membrane potentials
194 (Rm) was able to initiate rebound firing or rebound repetitive firing in most PVH^{BDNF} neurons
195 (**Figure 3—figure supplement 1A**). Hyperpolarization-induced I_H currents and low
196 depolarization events were observed in some PVH^{BDNF} neurons (**Figure 3—figure supplement**
197 **1A**). cKO PVH^{BDNF} neurons showed reduced action potential (AP) firing frequency at a holding
198 voltage of -60mV compared to Ctrl PVH^{BDNF} neurons (**Fig 3B-C**). The resting membrane
199 potential (Rm) of cKO (-52mV) neurons showed a 10mV positive shift compared to Ctrl neurons
200 (-62mV) (**Fig 3D**). We also found that fewer cKO PVH^{BDNF} neurons showed spontaneous firing
201 at Rm (**Fig 3E**, Ctrl:10/13; cKO:5/12) and at a holding voltage of -70mV (**Fig 3F**, Ctrl:6/12;
202 cKO:1/12) compared to Ctrl PVH^{BDNF} neurons. The threshold of the first AP initiated by a ramp
203 current injection (1 nA/sec) from Rm was significantly increased in cKO neurons (**Fig 3G-H**).
204 Because a wider shoulder and lower AP amplitude were observed when held at more depolarized
205 potentials (**Figure 3—figure supplement 1B**), we compared the AP waveforms at a holding
206 voltage of -60mV, close to the Rm of both genotypes. The AP of the cKO group exhibited a
207 lower peak amplitude (measuring from the threshold to peak) (**Fig 3I**), a normal threshold (**Fig**
208 **3J**), and a normal half-width (**Figure 3—figure supplement 1C**). In summary, we found that
209 both passive and AP properties of cKO PVH^{BDNF} neurons were altered due to RAI1 loss. The

210 Rm of cKO neurons shifted to a more positive voltage than the gating threshold of voltage-gated
211 sodium channels (6/12 were more positive than -55mV), which was unfavourable for their
212 transition from the inactivation state to the closed state. Combined with the higher AP threshold
213 of cKO neurons, these changes contribute to a decreased excitability in cKO PVH^{BDNF} neurons.

214 PVN neurons receive glutamatergic and GABAergic inputs and are tonically inhibited by
215 GABAergic neurons (Colmers & Bains, 2018; Gao *et al*, 2017). We observed a slight rightward
216 shift of the probability of miniature inhibitory postsynaptic current (mIPSC) frequency in cKO
217 PVH^{BDNF} neurons, although the average frequency (**Fig 3K**) was not significantly different
218 between groups. The probability of mIPSC amplitude also showed a right shift without a
219 significant change (**Fig 3L, Figure 3—figure supplement 1D**). However, we observed a
220 significantly increased area under the curve (**Fig 3M**). Interestingly, we found that cKO
221 PVH^{BDNF} neurons had a smaller cellular diameter (**Figure 3—figure supplement 1E**). Overall,
222 our data argue that *Rai1* deletion decreases the excitability and AP firing of PVH^{BDNF} neurons
223 without significant changes in synaptic inhibitory transmission.

224

225 **RAI1 is necessary for PVH^{BDNF} neurons to regulate energy homeostasis**

226 Reduced PVH^{BDNF} neuronal activity in cKO mice suggested that RAI1 loss in BDNF-producing
227 PVH neurons might be sufficient to induce defective energy homeostasis *in vivo*. To test this
228 hypothesis by deleting *Rai1* only in PVH^{BDNF} neurons but not other BDNF-producing cells, we
229 performed PVH^{BDNF}-specific *Rai1* deletion using a CRISPR/Cas9 system packaged into AAV9.
230 Two viruses were delivered: one encoding a reporter molecule (GFP) and three single guide
231 RNAs targeting the *Rai1* gene (*sgRai1*), and the other carrying Cre-dependent *Staphylococcus*
232 *aureus* CRISPR-associated protein 9 (saCas9) (**Fig 4A**). Hereafter, our experiments focus on

233 female SMS mice since they showed more consistent defects in fat distribution (Burns *et al.*,
234 2010) and body weight regulation (Huang *et al.*, 2016) than males. Bilateral administration of
235 two AAVs into the PVH of female *Bdnf*$^{Cre/+}$ mice (Exp group) at 3 weeks of age resulted in a
236 significant loss of Rai1 protein expression in PVH^{BDNF} neurons when compared to *Bdnf*$^{Cre/+}$ mice
237 injected with an AAV encoding the sgRai1 and GFP (Ctrl group) (**Fig 4B-C**, **Figure 4—figure**
238 **supplement 1A**). Quantification of AAV-infected (GFP^{+}) BDNF neurons showed that while the
239 total number of BDNF^{+} (**Figure 4—figure supplement 1B**) and BDNF^{+} GFP^{+} (**Figure 4—**
240 **figure supplement 1C**) cells were not different in the two groups, the percentage of AAV-
241 infected BDNF^{+} cells that express RAI1 was significantly reduced in the Exp group (**Fig 4C**,
242 **Figure 4—figure supplement 1D-E**). Moreover, the virus expression did not spread to the non-
243 PVH neighboring nuclei (**Figure 4—figure supplement 1F**). Deleting *Rai1* from the PVH^{BDNF}
244 neurons resulted in a significant increase in body weight beginning at 17 weeks of age (**Fig 4D**).
245 Similar to the cKO (*Bdnf*$^{Cre/+}$*; Rai1*$^{fl/fl}$) mice, obesity in 26-week-old Exp mice was due to
246 increased fat mass (**Fig 4E**) and more specifically, increased subcutaneous inguinal (S.C. ing)
247 and epididymal white adipose tissues (eWAT) but not BAT (**Fig 4F**). We also found that eWAT
248 adipocytes became hypertrophic (**Fig 4G**). Similar to the cKO mice, food intake did not differ
249 between Exp and Ctrl groups (**Fig 4H**), likely due to the high level of satiety signals in the brain
250 caused by increased blood leptin levels (**Fig 4I**). We also found that energy expenditure (**Fig 4J**),
251 respiratory exchange rate (**Figure 4—figure supplement 1G**), and blood lipid parameters,
252 including TG (**Figure 4—figure supplement 1H**), HDL (**Figure 4—figure supplement 1I**),
253 LDL and VLDL levels (**Figure 4—figure supplement 1J**), were similar in Exp and Ctrl groups,
254 consistent with the cKO data (**Figure 2**). Interestingly, Exp mice showed significantly less
255 locomotor activity during the dark phase than the Ctrl mice (**Fig 4K**). A GTT indicated that Exp

256 mice have a hyperglycemic profile (**Fig 4L**), accompanied by a slightly higher area under the
257 curve for blood glucose levels (p=0.05) (**Fig 4M**). Insulin levels in Exp mice were also
258 significantly elevated 15 minutes after glucose administration (**Fig 4N**).

259 While Exp mice showed a trend towards increased glucose levels in insulin tolerance tests, the
260 change was not statistically different (**Figure 4—figure supplement 1K**). Altogether, these
261 experiments indicate that conditional deletion of *Rai1* from PVH^{BDNF} neurons during
262 adolescence impairs the regulation of body weight, adiposity, glucose tolerance, and locomotion.
263 These changes recapitulate most phenotypes observed in cKO mice with *Rai1* deleted in BDNF-
264 producing cells from early development.

265

266 **Pharmacologically enhancing neurotrophin downstream signalling partially alleviates**
267 **obesity in SMS mice**

268 Our findings so far indicate that multiple pathways, including neurotrophin signalling, are
269 dysregulated in SMS mice, and that Rai1 loss from BDNF-producing cells, including PVH^{BDNF}
270 neurons, impairs energy homeostasis *in vivo*. Next we sought to examine the contribution of
271 BDNF dysfunction in SMS pathogenesis by pharmacologically activating downstream targets of
272 the neurotrophin pathway.

273 We systematically treated mice with LM22A-4, a potential small molecule BDNF loop domain
274 mimetic (Massa *et al*, 2010). To measure the bioavailability of LM22A-4 in the SMS brain, we
275 simultaneously administered LM22A-4 intranasally (5 mg/kg body weight) and intraperitoneally
276 (50 mg/kg body weight), using the highest doses used in previous studies (Canals *et al*, 2004;
277 Chang *et al*, 2006; Gu *et al*, 2022; Kron *et al*, 2012; Ogier *et al*, 2007). We then harvested

278 forebrain and hypothalamic tissues one or three hours after drug administration. The
279 spectrometric analysis found a significantly higher LM22A-4 concentration in both brain regions
280 one-hour post-treatment, while its concentration decreased three hours after treatment (**Figure**
281 **5—figure supplement 1A**). Consistent with the reduced neurotrophin signalling observed in our
282 proteomic analysis, saline-treated SMS mice showed reduced phosphorylated-AKT (p-AKT; **Fig**
283 **5A**, **Figure 5—figure supplement 1B**) levels in the hypothalamus. LM22A-4 treatment
284 significantly increased the levels of p-AKT in the SMS mice 1-hr post-treatment (**Fig 5A**, **Figure**
285 **5—figure supplement 1B**), indicating increased signalling downstream of the BDNF pathway.

286 We next examined if chronic LM22A-4 treatment was sufficient to reverse or modify the
287 progression of the obesity phenotype in adult SMS mice. Specifically, we treated SMS mice
288 daily from 8 to 14 weeks of age, during which SMS mice began to gain significantly more
289 weight. Saline-treated SMS mice (**Fig 5C**) were significantly heavier than saline-treated control
290 mice from 9 weeks of age onward. Interestingly, LM22A-4-treated SMS mice showed a similar
291 body weight to saline-treated control littermates until 13 weeks of age but became obese by 14
292 weeks of age (**Fig 5D**). Consistent with a partial rescue, LM22A-4-treated SMS mice were
293 significantly less obese than saline-treated SMS mice throughout the treatment period (**Fig 5E**).
294 Control mice treated with LM22A-4 did not show a further reduction in body weight (**Figure**
295 **5—figure supplement 1C**), indicating that the therapeutic effects were specific to SMS
296 pathogenesis.

297 We measured food intake and found that LM22A-4 did not significantly rescue increased food
298 intake in SMS mice (**Fig 5F**). SMS mice showed normal energy expenditure (**Figure 5—figure**
299 **supplement 1D**) and respiratory exchange rate (**Figure 5—figure supplement 1E**), neither of
300 which was altered by LM22A-4 treatment. Interestingly, we did observe a partial rescue of

301 locomotor activity in LM22A-4-treated SMS mice that was not significantly different from
302 saline-treated Ctrl or SMS mice (**Fig 5G**). We also found that the LM22A-4 treatment partially
303 rescued fat deposition (**Fig 5H**) and completely rescued HDL levels (**Fig 5I**) in SMS mice.
304 During an insulin tolerance test, we found that saline-treated SMS mice showed increased
305 baseline insulin levels (**Fig 5J**) and blood glucose levels during the test (**Fig 5K**), both of which
306 were partially rescued by LM22A-4 treatment.

307 In addition to a deficit in energy homeostasis, SMS mice showed two highly reproducible
308 behavioural deficits: increased stereotypic rearing in the open field and decreased social
309 dominance in the tube test (Huang *et al*, 2018; Rao *et al*, 2017). Saline-treated SMS mice
310 showed significantly more rearing behaviour when compared to the saline-treated controls (**Fig**
311 **5L**). Interestingly, the LM22A-4 treatment reduced the repetitive rearing behaviour in SMS mice
312 **(Fig 5L**). LM22A-4 treatment did not change repetitive behaviours in control mice (**Figure 5—**
313 **figure supplement 1F**), suggesting the effect is specific to *Rai1* haploinsufficiency. However,
314 we did not observe a rescue of social dominance deficits in SMS mice (**Figure 5—figure**
315 **supplement 2A-E**). Together, these data indicate that LM22A-4 treatment delayed the onset of
316 obesity and fully rescued repetitive behaviour in SMS mice, suggesting that neurotrophin
317 downstream signalling dysfunction contributes to changes in the mouse SMS brain linked to
318 obesity and behavioural phenotypes.

319

320 **Discussion**

321 The hypothalamus and neurotrophin signalling in this region control body weight by regulating
322 the intricate balance between energy intake and expenditure (Xu & Xie, 2016). The role of
323 BDNF-producing neurons in human obesity disorders and how the activity of these cells is

324 regulated remained poorly studied. We found that *Rai1* deficiency, linked to Smith-Magenis
325 syndrome (SMS), regulates BDNF expression and maintains intrinsic excitability in PVH^{BDNF}
326 neurons.

327 Consistent with this mechanism, we found that removing RAI1 from BDNF-producing neurons
328 or PVH^{BDNF} neurons results in imbalanced energy homeostasis and obesity. A small molecule
329 drug LM22A-4 led to increased AKT phosphorylation and partially rescued locomotor activity,
330 insulin intolerance, and HDL levels, while delaying the onset of obesity in SMS mice. These
331 findings highlight a potential role for hypothalamic BDNF-producing neurons, specifically
332 PVH^{BDNF} neurons, in SMS pathogenesis and highlight BDNF signalling as a potentially
333 druggable pathway to improve energy homeostasis defects and repetitive behaviours commonly
334 observed in SMS patients (Burns *et al.*, 2010; Moss *et al*, 2009).

335 The involvement of different PVH subtypes in human obesity is only beginning to be elucidated.
336 Dysfunction of oxytocin PVH neurons is linked to the Prader-Willi syndrome (Lee *et al*, 2012),
337 another genetic disorder associated with obesity. Since *Rai1* expression is enriched in PVH^{BDNF}
338 neurons but not $PVH^{Oxytocin}$ neurons, our data suggest that distinct pathophysiological
339 mechanisms underlie SMS and Prader-Willi syndrome.

340 The conditional knockout analysis allowed us to precisely map the cell-specific origin of
341 neuropathological phenotypes, such as SMS-like symptoms in mice. Our previous work found
342 that deleting *Rai1* from cortical excitatory neurons using an $Emx1^{Cre}$ allele (Gorski *et al*, 2002),
343 from the GABAergic neurons using a $Gad2^{Cre}$ allele (Taniguchi *et al*, 2011), or from astrocytes
344 using a $Gfap^{Cre}$ allele (Garcia *et al*, 2004) did not induce SMS-like obesity (Huang *et al.*, 2016).
345 In contrast, obesity could be induced by ablating *Rai1* from Sim1-lineage neurons and, to a lesser
346 extent, SF1-lineage neurons (Huang *et al.*, 2016). This analysis suggests that Rai1 expression in

347 PVH is more important than in the ventromedial nucleus of the hypothalamus (VMH) for body
348 weight regulation. Interestingly, Although BDNF is required in the VMH and DMH to regulate
349 body weight (Unger *et al.*, 2007), embryonic deletion of *Bdnf* from the SF1-lineage populations
350 including the VMH did not result in obesity (Kamitakahara *et al*, 2016; Yang *et al*, 2016). By
351 contrast, deleting *Bdnf* from Sim1-lineage neurons including the PVH resulted in a more severe
352 obesity phenotype (An *et al.*, 2015). This is consistent with the idea that BDNF expression in
353 PVH is critical for energy homeostasis. We found that *Rai1* expression in BDNF-producing cells
354 regulates energy homeostasis in a sexually dimorphic manner. Specifically, female cKO mice
355 showed normal food intake, decreased energy expenditure, and reduced locomotor activity. In
356 contrast, male cKO mice showed increased food intake with no changes in locomotor activity.
357 Intriguingly, energy expenditure was increased in male cKO mice, likely due to the higher
358 demand to maintain normal activity levels in obese mice. In both sexes, cKO mice showed an
359 increased fat mass and adiposity with no change in lean mass, highlighting an essential role for
360 Rai1 in regulating fat deposition. Our data also indicate that BDNF-producing cells are only
361 partially responsible for obesity in SMS: male and female cKO mice become overweight by 15
362 weeks, in contrast to SMS mice which become obese by 9 weeks of age, suggesting that non-
363 BDNF neurons contribute to SMS phenotypes.

364 Notably, mice lacking one copy of *Rai1* in the BDNF-producing cells do not exhibit
365 obesity, whereas SMS patients and SMS mice show pronounced obesity (Burns *et al.*, 2010;
366 Huang *et al.*, 2016; Smith *et al*, 2005). This indicates that although reduced *Bdnf* expression and
367 BDNF-producing neurons contribute to regulating body weight, additional molecular changes
368 and other hypothalamic populations also play important roles in regulating body weight
369 homeostasis in SMS. Our RPPA data suggest that mTOR signalling is also misregulated in

370 addition to the reduced activation of the neurotrophin downstream cascades. Hypothalamic
371 mTORC1 is crucial to regulate glucose release from the liver, peripheral lipid metabolism, and
372 insulin sensitivity (Burke *et al*, 2017; Caron *et al*, 2016; Smith *et al*, 2015), while mTORC2
373 regulates glucose tolerance and fat mass (Kocalis *et al*, 2014). How the impaired mTOR
374 signalling contributes to energy homeostasis defects in SMS and the therapeutic potential of
375 targeting this pathway to treat SMS-related obesity remains unclear and warrants future
376 investigation.

377 What additional RAI1-dependent hypothalamic cell types residing in brain regions other than
378 PVH regulate obesity in SMS? Other important cell types such as TRKB neurons within the
379 PVH (An *et al*, 2020) and several RAI1-expressing hypothalamic nuclei including the arcuate
380 nucleus, ventromedial nucleus of the hypothalamus (VMH), and lateral hypothalamus all play
381 important roles in regulating energy homeostasis. POMC- and AGRP-expressing neurons within
382 the arcuate nucleus are known to regulate food intake and glucose and insulin homeostasis
383 (Quarta *et al*, 2021; Vohra *et al*, 2022). Therefore, *Rai1* function in these neurons could
384 contribute to obesity in SMS, a topic that awaits future investigation.

385 We found the metabolic phenotypes induced by deleting *Rai1* from BDNF-producing cells were
386 specifically due to *Rai1* deletion in PVH^{BDNF} neurons. Therefore, our study focused on PVH^{BDNF}
387 neurons. Electrophysiological experiments showed that most wild-type PVH^{BDNF} neurons display
388 high-frequency spontaneous AP firing (1-10 Hz) at the resting membrane potential. Most
389 PVH^{BDNF} neurons fire sharp APs held at a hyperpolarized potential and show repetitive
390 overshoot during the current ramp test. Loss of *Rai1* significantly reduced the intrinsic neuronal
391 excitability of PVH^{BDNF} neurons. Because GABAergic *Rai1* loss did not induce obesity (Huang
392 *et al.*, 2016) and most BDNF-producing neurons are glutamatergic (Canals *et al*, 2001). The

393 ionic changes in PVH^{BDNF} neurons that precisely explain these excitability changes await future
394 investigations. Different groups of PVH neurons show phasic bursting or slowly inactivating
395 delayed rectifier potassium conductance, which are properties mediated by different potassium
396 channels (Lee *et al.*, 2012). Given that our previous RNA-seq experiment found that
397 hypothalamic Rai1 loss induces misexpression of potassium channel subunits *KCNC2* and
398 *KCNJ11* (Huang *et al.*, 2016), RAI1-dependent potassium channels are likely involved in altered
399 neuronal activity. Furthermore, we found fewer low threshold depolarization events in cKO
400 PVH^{BDNF} neurons during the hyperpolarized voltage step, suggesting a potential involvement of
401 HCN channels.

402 Our previous work found that *Rai1* loss in the dentate gyrus resulted in neuronal
403 hyperexcitability (Chang *et al*, 2022b). Here we demonstrated that *Rai1* loss in the hypothalamus
404 resulted in neuronal hypoactivity, suggesting that RAI1 regulates neuronal excitability in a cell
405 type-specific manner. Reduced PVH^{BDNF} neuronal activity upon *Rai1* loss could potentially
406 explain obesity, consistent with a previous report that found chemogenetic activation of
407 PVH^{BDNF} neurons promotes negative energy balance by decreasing feeding and increasing
408 energy expenditure (Wu & Xu, 2022).

409 It is plausible that RAI1 regulates the expression of genes encoding inward rectifier K^+ channels,
410 which regulate neuronal activity and potentially energy homeostasis. For instance, KIR6 (a
411 family of ATP-sensitive potassium channels, K_{ATP}) is widely expressed in the hypothalamus.
412 Deleting the hypothalamic KIR6.2 subunit impairs K_{ATP} channel function and glucose tolerance
413 (Miki *et al*, 2001; Parton *et al*, 2007). Moreover, reduced expression of hypothalamic GIRK4
414 (encoding an inwardly rectifying potassium channel) causes obesity (Perry *et al*, 2008).
415 GABAergic neurotransmission from arcuate AGRP-expressing neurons to the PVH neurons is

important to increase appetite by favouring hyperphagia (Atasoy *et al*, 2012). Disrupting the composition of these ion channels could contribute to reduced PVH^{BDNF} neuronal firing, which awaits further investigations.

Female mice with a conditional knockout of *Rai1* from BDNF-producing neurons do not display a noteworthy difference in food intake. Conversely, their male counterparts exhibit a significant increase in food intake. Although SMS individuals of both genders tend to overeat, male patients who are obese show significantly higher food consumption than their female counterparts (Gandhi *et al.*, 2022). This observation raises the possibility that *Rai1* regulates eating behaviours through multiple cell types in the hypothalamus and that a male-specific involvement of BDNF-producing neurons in regulating food intake, potentially provides a neurobiological basis for the observed pattern in SMS patients (Gandhi et al., 2022). In future work, it would be interesting to dissect the sex-specific role of RAI1 in regulating the functional development of PVH^{BDNF} neurons. In addition to a role for RAI1 in regulating neuronal activity, RAI1 may regulate other aspects of PVH^{BDNF} neuronal function, including projections to other brain regions to regulate energy homeostasis. In this regard, it would be interesting to dissect how RAI1 controls the circuit connectivity of PVH^{BDNF} neurons and how *Rai1* loss in PVH^{BDNF} neurons affects nearby PVH^{TRKB} neurons that receive BDNF signalling and are linked to body weight regulation (An *et al.*, 2020).

At the molecular level, our RPPA data show that *Rai1* depletion disrupted multiple intracellular signalling pathways and resulted in the hypoactivation of specific phospho-signalling proteins. Multiple early studies support the notion that Rai1 directly promotes *Bdnf* expression. First, hypothalamic *Bdnf* mRNA levels were reduced in SMS mice (Burns *et al.*, 2010; Javed *et al.*, 2021) or mice with *Rai1* conditional deletions (Huang *et al.*, 2016). Second, the RAI1 protein

439 directly binds to a promoter region of *Bdnf* (Huang *et al.*, 2016). Finally, when *Rai1* expression
440 was induced using CRISPR activation, *Bdnf* mRNA levels were significantly elevated (Chang *et*
441 *al*, 2022a).

442 To lend further support, here we show that SMS mice have reduced hypothalamic BDNF
443 protein levels, as well as reduced activation of a TRKB downstream target AKT. Reduced AKT
444 activity is frequently associated with insulin resistance and obesity in mice (Shao *et al*, 2000) and
445 children (Su *et al.*, 2021). We also found that obesity, increased HDL levels, and insulin
446 insensitivity in SMS mice could be partially alleviated using a small molecule drug (LM22A-4)
447 that promotes AKT phosphorylation. LM22A-4 penetrates the blood-brain barrier reasonably
448 well and has been shown to ameliorate symptoms of other neurological disorders associated with
449 BDNF dysfunction including Rett syndrome, Huntington's disease, Dravet syndrome, and
450 refractory neonatal seizures (Canals *et al.*, 2004; Chang *et al.*, 2006; Gu *et al.*, 2022; Kron *et al.*,
451 2012; Ogier *et al.*, 2007). We recognize that while several in vivo studies have demonstrated the
452 potential of LM22A-4 in targeting neurotrophin downstream signalling (Kron *et al*, 2014; Li *et*
453 *al*, 2017), an in vitro analysis failed to demonstrate the ability of LM22A-4 to activate TRKB
454 directly (Boltaev *et al*, 2017). Therefore, the precise mechanism by which LM22A-4 enhances
455 AKT cascades in the mammalian brain remains unclear and awaits further investigations. In the
456 hypothalamus of SMS mice, LM22A-4 could indirectly engage neurotrophin downstream PI3K-
457 AKT pathway through the G protein-coupled receptor-dependent transactivation of the TRKB
458 receptor (Domeniconi & Chao, 2010) or other unknown mechanisms. Moreover, while LM22A-
459 4 may have potential side effects, we found that wild-type mice treated with LM22A-4 did not
460 show a further decrease in body weight, suggesting limited side effects regarding body weight
461 regulation.

462 The partial rescue of SMS phenotypes that we observed contrasts with our previous findings that
463 found (1) AAV-mediated BDNF overexpression in PVH at 3 weeks of age and (2) genetically
464 overexpressing BDNF from early development could fully prevent the development of obesity in
465 SMS mice (Javed *et al.*, 2021). Therefore, further increasing TRKB signalling activation and
466 earlier intervention might improve therapeutic outcomes. Alternatively, our RPPA data showed
467 that in addition to disruption of neurotrophin signalling, multiple pathways including mTOR
468 were downregulated in SMS. Increasing hypothalamic mTOR activity has been shown to
469 decrease food intake and body weight (Cota *et al.*, 2006). Therefore, it is possible that enhancing
470 both mTOR and TRKB signalling could achieve a more robust rescue of obesity in SMS mice.
471 Nevertheless, these data support the concept that drugging TRKB signalling may improve
472 stereotypical repetitive behaviour and partially alleviate metabolic functions in a mouse model of
473 SMS. Delayed symptom onset could provide a window of opportunity for other interventions to
474 further modify disease progression, an area requiring further investigation.

475 This study has several limitations. First, whether the PVH^{BDNF} neurons depend on Rai1 to
476 regulate adaptive thermogenesis awaits future analysis. It is known that a subset of posterior
477 PVH^{BDNF} neurons project to the spinal cord and regulate thermogenesis (An *et al.*, 2015).
478 However, we found the weights of brown adipocytes were similar in control and cKO mice.
479 Moreover, SMS mice have normal respiratory exchange rates and there are currently no reports
480 of defective adaptive thermogenesis in SMS patients. This suggests that adaptive thermogenesis
481 is not impacted in SMS. Another limitation is that we did not test different doses, durations, and
482 time points for LM22A-4 treatment. The precise mechanisms by which LM22A-4 improves
483 body weight, metabolic function, and repetitive behaviours remain unknown. Nevertheless, our
484 work identifies RAI1 as a novel regulator of the neuronal excitability of PVH^{BDNF} neurons. This

485 regulation is critical for regulating food intake and energy expenditure. Our evidence suggests
486 that BDNF-producing neurons are involved in SMS pathogenesis and that enhancing BDNF-
487 TRKB signalling should be explored as a future therapeutic avenue for obesity and metabolic
488 conditions associated with reduced neurotrophin signalling (Xu & Xie, 2016).
489
490

491 **Materials and Methods**

492 **Animal Management**

493 The animal protocol was approved by the animal care committee of the Montreal General
494 Hospital and was performed according to the guidelines of the Canadian Council on Animal
495 Care. Mice were group-housed in 12-hour light/12-hour dark cycles with an *ad libitum* supply of
496 regular chow and water. The exception was in the fasting studies when the animals were food
497 deprived for 5 hours and in CALMS and food intake studies when animals were single-housed in
498 a 12-hour light/12-hour dark cycle with an *ad libitum* supply of regular chow and water. All mice
499 were maintained in a C57Bl/6J background. *Bdnf*$^{Cre/Cre}$, *Rosa-tomato*$^{td/td}$ (Ai9), and *Actβ*$^{Cre/Cre}$
500 mice were purchased from the Jackson laboratory. The *Rai1*$^{fl/fl}$ strain was previously generated
501 and characterized by us (Huang *et al.*, 2016). SMS mice (*Rai1*$^{+/-}$: whole-body germline *Rai1*
502 heterozygous knockout that genetically mimics SMS) were generated by crossing germline
503 *Actβ*$^{Cre/Cre}$ mice with *Rai1*$^{fl/+}$. To generate conditional knockout mice, *Bdnf*$^{Cre/+}$; *Rai1*$^{fl/+}$ mice
504 were crossed with *Rai1*$^{fl/+}$ to create control and experimental groups from the same littermate.

505

506 **Metabolic profiling**

507 Metabolic profiling was conducted in three experimental conditions: male and female
508 conditional knockout mice, female virus-injected *Bdnf*$^{Cre/+}$ mice, and female drug- or saline-
509 injected SMS and control mice. Metabolic profiling included body weight and body composition
510 analysis, food intake measurement, indirect calorimetry for locomotion activity, energy
511 expenditure (EE), respiratory exchange rate (RER), measurement of serum lipids and leptin
512 levels, adipose tissue histology analysis, and glucose and insulin tolerance tests. All experiments

513 were performed as previously described (Javed *et al.*, 2021). A brief description is detailed
514 below.

515

516 *Body weight and body composition analysis*

517 The body weight of animals was measured weekly from week 3 (weaning age) onward. After the
518 25th week, mice were subjected to body composition analysis. Body composition, including total
519 fat and lean mass, was assessed using a nuclear EchoMRI whole-body analyzer. Toward the end
520 of the experiments, animals were euthanized to collect brown adipose, visceral, subcutaneous
521 (inguinal) and ependymal white adipose tissues and weighed using an analytical scale
522 (Sartorius).

523

524 *Food Intake Measurement*

525 Mice were single-housed for food intake measurement. Food intake was measured over a one-
526 week period during which food was weighed prior to placement in the cage with minimal
527 bedding. Each morning, the remaining food inside the cage was weighed. The amount of total
528 food consumed was averaged over 7 days.

529

530 *Indirect Calorimetry*

531 A Comprehensive Lab Animal Monitoring System (CLAM) (Columbus instruments) was used to
532 measure the RER and EE (normalized over lean mass). Animals were singled-housed in the

533 CLAMS apparatus at 21˚C (70˚F) in a light–dark cycle matching their housing conditions for 24
534 hours (acclimation), followed by 48 hours of measurement.

535

536 *Serum lipid level determination*

537 A fluorescence-based assay kit (Abcam ab65390) was used to measure serum lipid levels. The
538 manufacturer's instructions were followed except that we used half-area black 96-well
539 microplates. Fluorescence measurements at 535/587 nm (Ex/Em) were recorded with the Ensight
540 instrument from PerkinElmer. A new standard curve ranging from 0 to 10 µg/ml was produced
541 for each microplate to accurately determine lipid levels in serum samples. Standards and samples
542 were loaded and analyzed twice.

543

544 *Histology of adipose tissue*

545 Ependymal white adipose tissues (WAT) were excised immediately after the animals were
546 euthanized and fixed with 10% formalin in PBS. The fixed tissues were dehydrated, embedded in
547 paraffin, and sectioned. Two 5-micrometre thick sections were taken from each animal and
548 stained with hematoxylin and eosin. Images of sections were then captured using an Aperio
549 ScanScope CS slide scanner at 20X optical magnification, and the resulting images were saved
550 in jpeg format using the ImageScope software. The images were manually cleaned to remove
551 non-adipose tissues such as lymph nodes. An automated method using the Adiposoft plugin
552 version 1.16 was utilized to determine adipocyte size and number from the jpeg images in Fiji
553 version 2.1.0/1.53c. The Adiposoft settings used excluded cells on edges and set a minimum and
554 maximum cell diameter of 20 and 300 µm, respectively. An experimental value of 2.49 µm per

555 pixel was determined using the Aperio scale bar and used for Adiposoft. To ensure accuracy, two
556 images from each animal were analyzed blindly, examining more than 1600 cells per mouse and
557 more than 9100 cells per condition. Adipocyte size frequencies were calculated using the
558 frequency function in Excel.

559

560 *Glucose and insulin tolerance tests*

561 For the glucose tolerance test, experimental mice were food deprived for 5 hours with *ad libitum*
562 water supply. A bolus of glucose (1.5g/kg of lean body weight) was then administered
563 intraperitoneally and glycemia was measured from tail vein blood samples using the Accu-chek
564 Performa glucometer at T0 (before the injection) as well as at 15, 30, 45, 60, 90 and 120 min
565 (after the injection). Tail vein blood samples were collected via a capillary for insulin assays at
566 T0, 15 and 30 min. For insulin tolerance tests, experimental mice were food-deprived for 5 hours
567 with *ad libitum* access to water. A bolus of insulin (1 U/kg of lean body weight) was
568 administered via an IP injection and glycemia was measured from blood sampled at the tail vein
569 using an Accu-chek Performa glucometer at T0 (before the injection), as well as at 15, 30, 45, 60,
570 90 and 120 min (after the injection). Tail vein blood samples were collected via a capillary for
571 insulin assays at T0.

572

573 **Stereotaxic Injections**

574 *Bdnf*$^{Cre/+}$ mice were anesthetized using isoflurane, and the ears were barred onto a stereotaxic
575 device (David Kopf Instruments). Adeno-associated viruses (AAVs, volume = 250 nl) were
576 bilaterally injected into the PVH using the following coordinates relative to the Bregma: -0.6 mm

577 anteroposterior (AP), ±0.35 mm mediolateral (ML) and -5.52 mm dorsoventral (DV). A
578 description of the AAV constructs and titre used is detailed below:

579 AAV9-CMV7-DIO-saCas9 (Viral title: >1 × 10^13), Vector Biolab

580 AAV9-CMV7-sgRai1-GFP (Viral title: >1 ×10^9), Applied Biological Materials Inc. Three
581 sgRNAs were pooled to target Rai1 (sgRNA1: TTCCTCGCCAGAGTAGCGCC, sgRNA2:
582 CCCAGCCTCATGATAGGCCG, sgRNA3: CCCAGCCTCATGATAGGCCG).

583

584 **Immunostaining of mouse brain tissues**

585 Immunostaining experiments were performed as previously described (Huang *et al*, 2012).
586 Briefly, mice were anesthetized and perfused with 1X PBS and 4% formaldehyde, and the brains
587 were dissected and fixed in 4% formaldehyde overnight. Fixed brains were transferred to 30%
588 sucrose solution and subsequently embedded in the OCT solution. The brains were then
589 sectioned (40µm), washed in PBS, permeabilized with 0.5% Triton X-100, and incubated with
590 10% normal donkey serum in PBS for 2 hours. The sections were then incubated overnight with
591 primary antibodies (Rai1: 1:500 dilution, RRID:AB_2921229 (Huang *et al.*, 2016); BDNF:
592 1:500, RRID:AB_10862052, Abcam ab108319; p-TRKB: 1:500 dilution, RRID:AB_2721199,
593 Millipore ABN1381; oxytocin: 1:1000 dilution, RRID:AB_11212999, Millipore MAB5296) at
594 4°C on a shaker. The following day, sections were washed with 1X PBS twice for 10 minutes
595 and incubated with a secondary antibody (1:1000 dilution) for 3 hours at room temperature.
596 Sections were washed with 1X PBS once before mounting on glass slides with the DAPI-
597 mounting (DAPI-Fluoromount-G, SouthernBiotech) and then imaged using a confocal
598 microscope (Olympus FV-1000 confocal laser scanning microscope) with 20x or 40x objectives

599 (NA 0.85 and 1.3, respectively). Z-stacks were taken with a step size of 1.0 µm with a 1024 x
600 1024 resolution. Images were acquired as a stack with at least 13 optical sections. Image analysis
601 was performed using the Fiji software.

602

603 **Real-Time Quantitative Reverse Transcription PCR (qRT-PCR)**

604 qRT-PCR was performed using mRNAs isolated from hypothalamic tissue samples. After the
605 isolation of total RNA, mRNAs were reverse-transcribed with the SuperScript III First-Strand
606 Synthesis System (Thermo-Fisher). Quantitative PCR reactions were conducted using SsoFast
607 EvaGreen Supermix on a Bio-Rad qPCR system.

608

609 **Enzyme-linked immunosorbent assay (ELISA)**

610 ELISA was performed using hypothalamic tissues from 7-week-old SMS mice to assess the
611 mature BDNF protein levels using a commercially available BDNF ELISA kit (Mature BDNF
612 Rapid ELISA Kit: Human, Mouse, Rat).

613

614 **Western blotting analysis**

615 Mice were quickly decapitated, brains were rapidly removed, and hypothalamic tissues were
616 collected, weighed, and snap-frozen with liquid nitrogen. Hypothalamic tissues were lysed using
617 a tissue lysis buffer containing RIPA buffer (5M NaCl, 1M PH 8.0 Tris HCl, 1% NP.40, 10%
618 $C_{24}H_{39}NaO_4$, and 20% SDS) and the Halt™ Protease and Phosphatase Inhibitor Cocktail
619 (Thermo-Fisher). Lysates were first sonicated on ice for 15 seconds and centrifuged at 10000

620 RPM at 4°C for 10 minutes. The supernatant was collected in a separate Eppendorf tube, and a
621 BCA assay was performed to quantify protein levels. Proteins were then separated using SDS-
622 PAGE gel and transferred onto nitrocellulose membranes. To determine the phosphorylation
623 levels of AKT, membranes were cut and blocked in 5% milk in tris-buffered saline (TBS) for 1
624 hour and then incubated overnight at 4°C with anti-p-AKT (Ser473) antibody (1:1000 dilution,
625 RRID: AB_2315049, Cell Signaling Technology 4060T) and anti-H3 antibody (internal control:
626 1:1000 dilution, RRID: AB_302613, Abcam ab1791). The next day, membranes were washed
627 with TBST three times for five minutes before incubating with an HRP-conjugated secondary
628 antibody (1:10000 dilution, Thermo Fisher 200-403-095S). Membranes were later stripped by
629 incubating in 0.5M NaOH for 10 min and then re-probed for total Akt levels by incubating with
630 anti-Akt (C67E7) antibody (1:1000 dilution, Cell Signaling Technology 4691T). The density of
631 each immunoreactive phospho-protein band was expressed as a fraction of the band for the total
632 AKT protein in the same lane.

633

634 **Reverse-phase protein array (RPPA)**

635 A reverse-phase protein array (RPPA) was used for precise high-throughput quantification of
636 total and phospho-protein levels in different signalling pathways. Protein lysates from
637 hypothalamic tissues were extracted and transferred to 384-well microarray plates to print
638 individual slides. The slides were then labelled with validated antibodies recognizing total
639 protein and specific phosphorylation sites. SYPRO Ruby staining was used to measure total
640 protein levels. The data obtained from RPPA were normalized for individual samples. Each
641 antibody's raw signal intensity (SI) was determined by subtracting the background from the
642 antibody-specific signals during image analysis. The normalized antibody SI was expressed

643 using the formula N = A - C/T x M, where N is the normalized SI, A is the raw antibody SI, C is
644 the negative control SI, T is the SI of total protein, and M is the median SI of total protein from a
645 spot within the same sample group. Antibodies with SI less than 200 were filtered out, and
646 quality control (QC) scores were established to discard poor-quality reactions. The coefficient of
647 variation (CV) score was determined for each antibody and defined as the percentage of samples
648 on a slide with a CV < 20%. Antibodies with a median technical triplicate CV >20% were also
649 excluded from further analysis. T-tests were performed for each antibody to identify
650 differentially expressed proteins in the SMS compared to control groups. PCA plots were
651 generated for all samples, annotated with their experimental group, and hierarchical clustering
652 was performed using a Python analysis tool. The vertical axis of the dendrogram represents the
653 dissimilarity (measured as distance) between protein expressions, and the horizontal axis
654 represents the individual test samples. The colour code (ranging from red to yellow to green)
655 specifies the expression levels of different proteins, where red indicates low expression, yellow
656 indicates intermediate expression, and green indicates high expression. Enrichment analysis on
657 the differentially expressed proteins was performed using an online data resource string: version
658 11.5.

659

660 **Electrophysiology of acute brain slices**

661 Mouse brains were removed and placed in ice-cold carbonated slicing artificial cerebrospinal
662 fluid (aCSF), which contained (in mM) 124 NaCl, 3 KCl, 1.4 NaH_2PO_4, 26 $NaHCO_3$,1.3 Mg
663 SO4, 10 D-glucose, 0.5 $CaCl_2$, and 3.5 $MgCl_2$. Coronal sections (300 µm) were cut on a
664 vibratome. Slices were allowed to recover at 32 °C for 40 minutes and then at 30 °C for
665 30 minutes to 6 hours in the recording medium, carbonated aCSF (124 NaCl, 3 KCl, 1.4

666 NaH_2PO_4, 26 $NaHCO_3$,1.3 Mg SO4, 10 D-glucose, 2.4 $CaCl_2$, in mM, ~300 mOsm). Signals
667 were recorded with a 5× gain, low-pass filtered at 2 kHz, digitized at 10 kHz (Molecular
668 Devices Multiclamp 700B) and analyzed with pClamp 11 (Molecular Devices). Whole-cell
669 recordings were made using 3–5 MΩ pipettes filled with an internal solution that contained
670 (in mM) 131 potassium gluconate, 8 NaCl, 20 KCl, 2 EGTA, 10 HEPES, 2 MgATP and 0.3
671 Na3GTP (pH 7.2, with KOH, 300–310 mOsm with sucrose). For miniature current recording,
672 the internal solution contained (in mM) 130 gluconate acid, 8 CsCl, 1 NaCl, 2 EGTA, 0.8
673 CsOH, 10 HEPES, 2 MgATP and 0.3 Na3GTP (pH 7.2, with CsOH, 300–310 mOsm adjusted
674 with sucrose). mEPSCs were recorded in the presence of 1 μM TTX at a holding potential of -
675 70 mV. mIPSCs were recorded at a holding potential of +10 mV. The mIPSCs were analyzed
676 from events during a 2-minute continuous recording that contained > 15 events/neuron.
677 Additional calculations, statistical analysis, and plotting were performed in Microsoft Excel or
678 Prism (GraphPad).

679

680 **Spectrometric analysis of LM22A-4 levels in the brain**

681 We assessed the efficacy of LM22A-4, a small molecule pharmacological agent, in 8-week-old
682 SMS and control mice. LM22A-4, chemical name N1, N3, N5tris (2hydroxyethyl) 1, 3, 5
683 benzenetricarboxamide (Molecular formula: $C_{15}H_{21}N_3O_6$, Formula weight: 339.3), was
684 manufactured by Cayman Chemical with purity specification >98%. A stock solution was made
685 by first dissolving LM22A-4 in DMSO (solubility =30mg/ml) and then diluting it with 0.9%
686 isotonic sterilized saline solution (Sigma). To maximize brain concentrations, LM22A-4 was
687 administered both intranasally (5mg/kg) and intraperitoneally (50mg/kg), as previously reported
688 (Simmons *et al*, 2013). The bioavailability of this drug in the hypothalamus using these doses

689 and routes of administration was assessed with the reverse phase LC triple-quadrupole tandem
690 mass spectroscopic detection (LC-MS/MS) by Absorption Systems. Mice were euthanized, and
691 hypothalamic tissue was collected at either 1 h or 3 h post-injection (n= 4/timepoint). Known
692 amounts of LM22A-4 were added to the blank sample to generate a standard curve to verify test
693 accuracy.

694

695 **LM22A-4 treatment**

696 Mice were divided into four groups: Saline-injected control, Saline-injected SMS, LM22A-4-
697 injected SMS, and LM22A-4-injected control mice. Mice were injected daily, intra-nasally
698 (5mg/kg) and intraperitoneally (50mg/kg), for 7 weeks. Body weight was measured between 8
699 and 14 weeks of age. Food intake was measured from 14 to 15 weeks of age. After 15 weeks of
700 age, mice were euthanized to collect brown adipose, visceral, subcutaneous (inguinal) and
701 ependymal white adipose tissues and weighed using an analytical scale (Sartorius).
702 Hypothalamic brain tissues were collected for western blot analysis. Metabolic profiling was
703 performed on a separate cohort of mice injected for two weeks prior to the start of experiments
704 as well as at specific weeks during the experiment.

705

706 **Vertical rearing**

707 To measure vertical repetitive rearing, mice were taken into the testing room and allowed to
708 habituate for 1 h prior to testing. During the test, mice were placed in the center of a 45 cm (W)
709 × 45 cm (D) × 40 cm (H) square arena, and their movement was recorded for 10 minutes.

Statistical analysis

The sample sizes used were based on our previous studies (Huang *et al.*, 2016; Javed *et al.*, 2021). The data were subjected to statistical analysis for significance by using GraphPad Prism 0.9. Significance was defined as having a p-value < 0.05. The significance levels were as follows: * p< 0.05, **p<0.01, ***p<0.0001, **** p<0.0001. The statistical tests used for each analysis (e.g., Student's t-test, analysis of variance [ANOVA]) are indicated in the text and legends.

Data Availability

This study includes no data deposited in external repositories.

Acknowledgements

Sehrish Javed was supported by a Fonds de Recherche du Québec - Santé (FRQS) doctoral award. This work was supported by the Rare Diseases: Models & Mechanisms Network and the Smith-Magenis syndrome Research Foundation.

Author contributions

Sehrish Javed: Conceptualization; formal analysis; investigation; data curation; visualization; writing. **Ya-Ting Chang**: Formal analysis; investigation; data curation; visualization. **Yoobin Cho**: Formal analysis; investigation. **Yu-Ju Lee**: Formal analysis; investigation. **Hao-Cheng Chang**: Formal analysis; investigation. **Minza Haque**: Formal analysis; investigation. **Yu Cheng Lin**: Formal analysis; investigation. **Wei-Hsiang Huang**: Conceptualization; supervision; funding acquisition; visualization; writing; project administration.

Disclosure and competing interests statement

The authors do not have any conflicts of interest to disclose relating to this work.

References

Abad C, Cook MM, Cao L, Jones JR, Rao NR, Dukes-Rimsky L, Pauly R, Skinner C, Wang Y, Luo F *et al* (2018) A Rare De Novo RAI1 Gene Mutation Affecting BDNF-Enhancer-Driven Transcription Activity Associated with Autism and Atypical Smith-Magenis Syndrome Presentation. *Biology (Basel)* 7

Alaimo JT, Barton LV, Mullegama SV, Wills RD, Foster RH, Elsea SH (2015) Individuals with Smith-Magenis syndrome display profound neurodevelopmental behavioral deficiencies and exhibit food-related behaviors equivalent to Prader-Willi syndrome. *Res Dev Disabil* 47: 27-38

An JJ, Kinney CE, Tan JW, Liao GY, Kremer EJ, Xu B (2020) TrkB-expressing paraventricular hypothalamic neurons suppress appetite through multiple neurocircuits. *Nat Commun* 11: 1729

An JJ, Liao GY, Kinney CE, Sahibzada N, Xu B (2015) Discrete BDNF Neurons in the Paraventricular Hypothalamus Control Feeding and Energy Expenditure. *Cell Metab* 22: 175-188

Atasoy D, Betley JN, Su HH, Sternson SM (2012) Deconstruction of a neural circuit for hunger. *Nature* 488: 172-177

Balthasar N, Dalgaard LT, Lee CE, Yu J, Funahashi H, Williams T, Ferreira M, Tang V, McGovern RA, Kenny CD *et al* (2005) Divergence of melanocortin pathways in the control of food intake and energy expenditure. *Cell* 123: 493-505

Boltaev U, Meyer Y, Tolibzoda F, Jacques T, Gassaway M, Xu Q, Wagner F, Zhang YL, Palmer M, Holson E *et al* (2017) Multiplex quantitative assays indicate a need for reevaluating reported small-molecule TrkB agonists. *Sci Signal* 10

Boot E, Linders CC, Tromp SH, van den Boogaard MJ, van Eeghen AM (2021) Possible underreporting of pathogenic variants in RAI1 causing Smith-Magenis syndrome. *Am J Med Genet A* 185: 3167-3169

Burke LK, Darwish T, Cavanaugh AR, Virtue S, Roth E, Morro J, Liu SM, Xia J, Dalley JW, Burling K *et al* (2017) mTORC1 in AGRP neurons integrates exteroceptive and interoceptive food-related cues in the modulation of adaptive energy expenditure in mice. *Elife* 6

Burns B, Schmidt K, Williams SR, Kim S, Girirajan S, Elsea SH (2010) Rai1 haploinsufficiency causes reduced Bdnf expression resulting in hyperphagia, obesity and altered fat distribution in mice and humans with no evidence of metabolic syndrome. *Hum Mol Genet* 19: 4026-4042

Canals JM, Checa N, Marco S, Akerud P, Michels A, Perez-Navarro E, Tolosa E, Arenas E, Alberch J (2001) Expression of brain-derived neurotrophic factor in cortical neurons is regulated by striatal target area. *J Neurosci* 21: 117-124

Canals JM, Pineda JR, Torres-Peraza JF, Bosch M, Martin-Ibanez R, Munoz MT, Mengod G, Ernfors P, Alberch J (2004) Brain-derived neurotrophic factor regulates the onset and severity of motor dysfunction associated with enkephalinergic neuronal degeneration in Huntington's disease. *J Neurosci* 24: 7727-7739

Caron A, Labbe SM, Lanfray D, Blanchard PG, Villot R, Roy C, Sabatini DM, Richard D, Laplante M (2016) Mediobasal hypothalamic overexpression of DEPTOR protects against high-fat diet-induced obesity. *Mol Metab* 5: 102-112

Chang HC, Lee YJ, Javed S, Haque M, Chang YT, Lin YC, Oram C, Huang WH (2022a) rAAV-CRISPRa therapy corrects Rai1 haploinsufficiency and rescues selective disease features in Smith-Magenis syndrome mice. *J Biol Chem*: 102728

Chang Q, Khare G, Dani V, Nelson S, Jaenisch R (2006) The disease progression of Mecp2 mutant mice is affected by the level of BDNF expression. *Neuron* 49: 341-348

Chang YT, Kowalczyk M, Fogerson PM, Lee YJ, Haque M, Adams EL, Wang DC, DeNardo LA, Tessier-Lavigne M, Huguenard JR *et al* (2022b) Loss of Rai1 enhances hippocampal excitability and epileptogenesis in mouse models of Smith-Magenis syndrome. *Proc Natl Acad Sci U S A* 119: e2210122119

784 Collaboration NCDRF (2017) Worldwide trends in body-mass index, underweight, overweight, and
785 obesity from 1975 to 2016: a pooled analysis of 2416 population-based measurement studies in 128.9
786 million children, adolescents, and adults. *Lancet* 390: 2627-2642
787 Colmers PLW, Bains JS (2018) Balancing tonic and phasic inhibition in hypothalamic corticotropin-
788 releasing hormone neurons. *J Physiol* 596: 1919-1929
789 Cota D, Proulx K, Smith KA, Kozma SC, Thomas G, Woods SC, Seeley RJ (2006) Hypothalamic mTOR
790 signaling regulates food intake. *Science* 312: 927-930
791 Domeniconi M, Chao MV (2010) Transactivation of Trk receptors in spinal motor neurons. *Histol*
792 *Histopathol* 25: 1207-1213
793 Edelman EA, Girirajan S, Finucane B, Patel PI, Lupski JR, Smith AC, Elsea SH (2007) Gender, genotype, and
794 phenotype differences in Smith-Magenis syndrome: a meta-analysis of 105 cases. *Clin Genet* 71: 540-550
795 Gandhi AA, Wilson TA, Sisley S, Elsea SH, Foster RH (2022) Relationships between food-related behaviors,
796 obesity, and medication use in individuals with Smith-Magenis syndrome. *Res Dev Disabil* 127: 104257
797 Gao H, Molinas AJR, Miyata K, Qiao X, Zsombok A (2017) Overactivity of Liver-Related Neurons in the
798 Paraventricular Nucleus of the Hypothalamus: Electrophysiological Findings in db/db Mice. *J Neurosci* 37:
799 11140-11150
800 Garcia AD, Doan NB, Imura T, Bush TG, Sofroniew MV (2004) GFAP-expressing progenitors are the
801 principal source of constitutive neurogenesis in adult mouse forebrain. *Nat Neurosci* 7: 1233-1241
802 Gorski JA, Talley T, Qiu M, Puelles L, Rubenstein JL, Jones KR (2002) Cortical excitatory neurons and glia,
803 but not GABAergic neurons, are produced in the Emx1-expressing lineage. *J Neurosci* 22: 6309-6314
804 Gray J, Yeo GS, Cox JJ, Morton J, Adlam AL, Keogh JM, Yanovski JA, El Gharbawy A, Han JC, Tung YC *et al*
805 (2006) Hyperphagia, severe obesity, impaired cognitive function, and hyperactivity associated with
806 functional loss of one copy of the brain-derived neurotrophic factor (BDNF) gene. *Diabetes* 55: 3366-
807 3371
808 Gu F, Parada I, Yang T, Longo FM, Prince DA (2022) Chronic partial TrkB activation reduces seizures and
809 mortality in a mouse model of Dravet syndrome. *Proc Natl Acad Sci U S A* 119
810 Huang WH, Guenthner CJ, Xu J, Nguyen T, Schwarz LA, Wilkinson AW, Gozani O, Chang HY, Shamloo M,
811 Luo L (2016) Molecular and Neural Functions of Rai1, the Causal Gene for Smith-Magenis Syndrome.
812 *Neuron* 92: 392-406
813 Huang WH, Tupal S, Huang TW, Ward CS, Neul JL, Klisch TJ, Gray PA, Zoghbi HY (2012) Atoh1 governs the
814 migration of postmitotic neurons that shape respiratory effectiveness at birth and chemoresponsiveness
815 in adulthood. *Neuron* 75: 799-809
816 Huang WH, Wang DC, Allen WE, Klope M, Hu H, Shamloo M, Luo L (2018) Early adolescent Rai1
817 reactivation reverses transcriptional and social interaction deficits in a mouse model of Smith-Magenis
818 syndrome. *Proc Natl Acad Sci U S A*
819 Javed S, Lee YJ, Xu J, Huang WH (2021) Temporal dissection of Rai1 function reveals brain-derived
820 neurotrophic factor as a potential therapeutic target for Smith-Magenis syndrome. *Hum Mol Genet* 31:
821 275-288
822 Javed S, Selliah T, Lee YJ, Huang WH (2020) Dosage-sensitive genes in autism spectrum disorders: From
823 neurobiology to therapy. *Neurosci Biobehav Rev* 118: 538-567
824 Kamitakahara A, Xu B, Simerly R (2016) Ventromedial hypothalamic expression of Bdnf is required to
825 establish normal patterns of afferent GABAergic connectivity and responses to hypoglycemia. *Mol Metab*
826 5: 91-101
827 Kocalis HE, Hagan SL, George L, Turney MK, Siuta MA, Laryea GN, Morris LC, Muglia LJ, Printz RL,
828 Stanwood GD *et al* (2014) Rictor/mTORC2 facilitates central regulation of energy and glucose
829 homeostasis. *Mol Metab* 3: 394-407

830 Kron M, Howell CJ, Adams IT, Ransbottom M, Christian D, Ogier M, Katz DM (2012) Brain activity
831 mapping in Mecp2 mutant mice reveals functional deficits in forebrain circuits, including key nodes in
832 the default mode network, that are reversed with ketamine treatment. *J Neurosci* 32: 13860-13872
833 Kron M, Lang M, Adams IT, Sceniak M, Longo F, Katz DM (2014) A BDNF loop-domain mimetic acutely
834 reverses spontaneous apneas and respiratory abnormalities during behavioral arousal in a mouse model
835 of Rett syndrome. *Dis Model Mech* 7: 1047-1055
836 Lee SK, Lee S, Shin SY, Ryu PD, Lee SY (2012) Single cell analysis of voltage-gated potassium channels that
837 determines neuronal types of rat hypothalamic paraventricular nucleus neurons. *Neuroscience* 205: 49-
838 62
839 Li W, Bellot-Saez A, Phillips ML, Yang T, Longo FM, Pozzo-Miller L (2017) A small-molecule TrkB ligand
840 restores hippocampal synaptic plasticity and object location memory in Rett syndrome mice. *Dis Model*
841 *Mech* 10: 837-845
842 Loos RJF, Yeo GSH (2022) The genetics of obesity: from discovery to biology. *Nat Rev Genet* 23: 120-133
843 Massa SM, Yang T, Xie Y, Shi J, Bilgen M, Joyce JN, Nehama D, Rajadas J, Longo FM (2010) Small molecule
844 BDNF mimetics activate TrkB signaling and prevent neuronal degeneration in rodents. *J Clin Invest* 120:
845 1774-1785
846 Miki T, Liss B, Minami K, Shiuchi T, Saraya A, Kashima Y, Horiuchi M, Ashcroft F, Minokoshi Y, Roeper J *et al*
847 (2001) ATP-sensitive K+ channels in the hypothalamus are essential for the maintenance of glucose
848 homeostasis. *Nat Neurosci* 4: 507-512
849 Moss J, Oliver C, Arron K, Burbidge C, Berg K (2009) The prevalence and phenomenology of repetitive
850 behavior in genetic syndromes. *J Autism Dev Disord* 39: 572-588
851 Ogier M, Wang H, Hong E, Wang Q, Greenberg ME, Katz DM (2007) Brain-derived neurotrophic factor
852 expression and respiratory function improve after ampakine treatment in a mouse model of Rett
853 syndrome. *J Neurosci* 27: 10912-10917
854 Parton LE, Ye CP, Coppari R, Enriori PJ, Choi B, Zhang CY, Xu C, Vianna CR, Balthasar N, Lee CE *et al* (2007)
855 Glucose sensing by POMC neurons regulates glucose homeostasis and is impaired in obesity. *Nature* 449:
856 228-232
857 Perry CA, Pravetoni M, Teske JA, Aguado C, Erickson DJ, Medrano JF, Lujan R, Kotz CM, Wickman K (2008)
858 Predisposition to late-onset obesity in GIRK4 knockout mice. *Proc Natl Acad Sci U S A* 105: 8148-8153
859 Quarta C, Claret M, Zeltser LM, Williams KW, Yeo GSH, Tschop MH, Diano S, Bruning JC, Cota D (2021)
860 POMC neuronal heterogeneity in energy balance and beyond: an integrated view. *Nat Metab* 3: 299-308
861 Rao NR, Abad C, Perez IC, Srivastava AK, Young JI, Walz K (2017) Rai1 Haploinsufficiency Is Associated
862 with Social Abnormalities in Mice. *Biology (Basel)* 6
863 Schultze SM, Hemmings BA, Niessen M, Tschopp O (2012) PI3K/AKT, MAPK and AMPK signalling: protein
864 kinases in glucose homeostasis. *Expert Rev Mol Med* 14: e1
865 Shao J, Yamashita H, Qiao L, Friedman JE (2000) Decreased Akt kinase activity and insulin resistance in
866 C57BL/KsJ-Leprdb/db mice. *J Endocrinol* 167: 107-115
867 Simmons DA, Belichenko NP, Yang T, Condon C, Monbureau M, Shamloo M, Jing D, Massa SM, Longo FM
868 (2013) A small molecule TrkB ligand reduces motor impairment and neuropathology in R6/2 and BACHD
869 mouse models of Huntington's disease. *J Neurosci* 33: 18712-18727
870 Slager RE, Newton TL, Vlangos CN, Finucane B, Elsea SH (2003) Mutations in RAI1 associated with Smith-
871 Magenis syndrome. *Nat Genet* 33: 466-468
872 Smith AC, Magenis RE, Elsea SH (2005) Overview of Smith-Magenis syndrome. *J Assoc Genet Technol* 31:
873 163-167
874 Smith AC, McGavran L, Robinson J, Waldstein G, Macfarlane J, Zonona J, Reiss J, Lahr M, Allen L, Magenis
875 E (1986) Interstitial deletion of (17)(p11.2p11.2) in nine patients. *Am J Med Genet* 24: 393-414

Smith MA, Katsouri L, Irvine EE, Hankir MK, Pedroni SM, Voshol PJ, Gordon MW, Choudhury AI, Woods A, Vidal-Puig A *et al* (2015) Ribosomal S6K1 in POMC and AgRP Neurons Regulates Glucose Homeostasis but Not Feeding Behavior in Mice. *Cell Rep* 11: 335-343

Su X, Gu D, Xu L, Liang Z, Luo X, Yang P, Yang J (2021) PI3K/Akt pathway expression in children with different obesity degrees and its relationship with glucolipid metabolism and insulin resistance. *Am J Transl Res* 13: 6592-6598

Tan CL, Cooke EK, Leib DE, Lin YC, Daly GE, Zimmerman CA, Knight ZA (2016) Warm-Sensitive Neurons that Control Body Temperature. *Cell* 167: 47-59 e15

Taniguchi H, He M, Wu P, Kim S, Paik R, Sugino K, Kvitsiani D, Kvitsani D, Fu Y, Lu J *et al* (2011) A resource of Cre driver lines for genetic targeting of GABAergic neurons in cerebral cortex. *Neuron* 71: 995-1013

Unger TJ, Calderon GA, Bradley LC, Sena-Esteves M, Rios M (2007) Selective deletion of Bdnf in the ventromedial and dorsomedial hypothalamus of adult mice results in hyperphagic behavior and obesity. *J Neurosci* 27: 14265-14274

Vohra MS, Benchoula K, Serpell CJ, Hwa WE (2022) AgRP/NPY and POMC neurons in the arcuate nucleus and their potential role in treatment of obesity. *Eur J Pharmacol* 915: 174611

Wu SW, Xu B (2022) Rapid and Lasting Effects of Activating BDNF-Expressing PVH Neurons on Energy Balance. *eNeuro* 9

Xu B, Goulding EH, Zang K, Cepoi D, Cone RD, Jones KR, Tecott LH, Reichardt LF (2003) Brain-derived neurotrophic factor regulates energy balance downstream of melanocortin-4 receptor. *Nat Neurosci* 6: 736-742

Xu B, Xie X (2016) Neurotrophic factor control of satiety and body weight. *Nat Rev Neurosci* 17: 282-292

Xu Y, Lu Y, Cassidy RM, Mangieri LR, Zhu C, Huang X, Jiang Z, Justice NJ, Xu Y, Arenkiel BR *et al* (2019) Identification of a neurocircuit underlying regulation of feeding by stress-related emotional responses. *Nat Commun* 10: 3446

Yang H, An JJ, Sun C, Xu B (2016) Regulation of Energy Balance via BDNF Expressed in Nonparaventricular Hypothalamic Neurons. *Mol Endocrinol* 30: 494-503

Yeo GS, Connie Hung CC, Rochford J, Keogh J, Gray J, Sivaramakrishnan S, O'Rahilly S, Farooqi IS (2004) A de novo mutation affecting human TrkB associated with severe obesity and developmental delay. *Nat Neurosci* 7: 1187-1189

908 **Figures and Figure legends**

909 **Figure 1: *Rai1* haploinsufficiency disrupts hypothalamic proteomic profile in mice**

910 **(A)** ELISA showing that BDNF protein levels in hypothalamic tissues were significantly reduced
911 in SMS mice compared to controls (n=4/genotype). *p<0.05, unpaired t-test, two-tailed.

912 **(B)** A schematic diagram showing the experimental strategy. Hypothalamic tissue lysates from 7-
913 week-old control (n = 5, technical triplicates/sample) and SMS (n=8, technical
914 triplicates/sample) mice were subjected to RPPA that utilizes a cocktail of 240 validated
915 antibodies to probe several key intracellular signalling pathways by quantifying the expression
916 levels of total and phosphorylated proteins

917 **(C)** Principal component analysis segregates the SMS and Ctrl groups where PC1 explains 47%
918 of the variance, and PC2 explains 25% of the variance.

919 **(D)** Heat map showing hierarchical clustering of differentially expressed phospho-proteins: most
920 showed reduced levels in SMS samples.

921 **(E)** Protein-protein interaction (PPI) analysis showing differentially expressed proteins and
922 phospho-proteins in a crosstalk network. PPI enrichment p-value: < 1.0e-16. The nodes represent
923 the proteins/phospho-proteins and the lines indicate physical interactions. Associations with
924 specific molecular pathways are shown as color-coded outer rings.

925 **(F-G)** The protein levels of two neurotrophin pathway-related nodes, PIK3CA (**F**) and phospho-
926 NF-kB (**G**), were significantly reduced in SMS samples. ****p<0.0001, unpaired t-test, two-
927 tailed

928

929 **Figure 2: RAI1 is required in BDNF-producing cells to regulate energy metabolism**

930 **(A)** A schematic diagram showing selective deletion of *Rai1* from BDNF-producing cells in
931 mice.

932 **(B)** Representative images showing that in Ctrl mice (*Bdnf*$^{Cre/+}$; *Ai9*), many PVH^{BDNF} neurons
933 (magenta) express RAI1 (cyan, double-positive cells were indicated with yellow arrows). By

934 contrast, PVH^{BDNF} neurons lack RAI1 expression in the cKO group (*Bdnf*$^{Cre/+}$; *Rai1*$^{fl/fl}$; *Ai9*).
935 Scale bars = 20µm.

936 **(C)** Percentage of PVH^{BDNF} neurons co-expressing RAI1 in Ctrl (n=3) and cKO (n=3) mice.
937 unpaired t-test, two-tailed, ****p<0.0001.

938 **(D)** Female cKO mice (n = 12) showed a significant weight gain when compared to female Ctrl
939 mice (n = 10). Two-way ANOVA with Šidák's multiple comparisons test. *p<0.05, ***p<0.001.

940 **(E)** Body composition was measured with Echo-MRI, showing an increased fat mass in 26-
941 week-old mice. ns indicates the difference is not significant. Two-way ANOVA with Šidák's
942 multiple comparisons test. ****p<0.0001.

943 **(F)** Fat mass of brown adipocytes (BAT), subcutaneous inguinal (S.C.ing) and epididymal white
944 adipose tissue (eWAT) in Ctrl and cKO mice. ns indicates the difference is not significant. Two-
945 way ANOVA with Šidák's multiple comparisons test. **p<0.01, ****p<0.0001.

946 **(G)** Representative images showing eWAT adipocyte hypertrophy of the cKO mice (left). Scale
947 bar = 500µm. Frequency distribution of adipocytes at each cellular size (right). Two-way
948 ANOVA with Šidák's multiple comparisons test. ***p<0.001, ****p<0.0001.

949 **(H)** Female cKO mice showed significantly increased blood leptin levels. unpaired t-test, two-
950 tailed, **p<0.01.

951 **(I)** Female cKO mice showed reduced energy expenditure during the dark phase. ns indicates not
952 significantly different. Two-way ANOVA with Šidák's multiple comparisons test. *p<0.05.

953 **(J)** Female cKO mice showed reduced locomotor activity during the dark phase. ns indicates the
954 difference is not significant. Two-way ANOVA with Šidák's multiple comparisons test. *p<0.05.

955 **(K)** Female cKO mice showed similar food intake as control mice. ns indicates not significant.
956 unpaired t-test, two-tailed.

957 **(L)** Glucose tolerance test showing that female cKO mice became hyperglycemic 20 minutes
958 after intraperitoneal glucose administration, suggesting glucose intolerance. Two-way ANOVA
959 with Šidák's multiple comparisons test. *p<0.05, ***p<0.001.

960 Data are shown as mean±SEM.

961

962

963 **Figure 3: *Rai1* loss reduces intrinsic neuronal excitability and enhances inhibitory synaptic**
964 **transmission of PVH^{BDNF} neurons**

965 **(A)** A representative image showing a patched PVH^{BDNF} neuron labelled by *Bdnf^{Cre}*-dependent
966 tdTomato fluorescence signals.

967 **(B-C)** Representative traces of spontaneous firing of control (black) and cKO (red) neurons at a
968 holding voltage of -60mV **(B)**. The average spontaneous AP firing frequencies are shown in **(C)**.
969 *p<0.05, unpaired student's t-tests.

970 **(D)** The resting membrane potentials of control (black) and cKO (red) PVH^{BDNF} neurons.
971 **p<0.01, unpaired student's t-tests.

972 **(E-F)** The number of control (black) and cKO (red) PVH^{BDNF} neurons that showed spontaneous
973 firing (open) or are silent (solid) at resting membrane potentials **(E)** and a holding voltage of -
974 70mV **(F)**.

975 **(G)** Representative traces of elicited APs in control (black) and cKO (red) PVH^{BDNF} neurons
976 responding to an inject current (bottom, blue), which ramps up from the resting membrane
977 potentials at 1 nA per second for 500ms.

978 **(H)** The threshold of the first AP initiated by a current ramp in control (black) and cKO (red)
979 PVH^{BDNF} neurons. *p<0.05, unpaired student's t-tests.

980 **(I-J)** The amplitude **(I)** and threshold **(J)** for the first AP firing at the holding voltage of -60mV
981 in control (black) and cKO (red) PVH^{BDNF} neurons. *p<0.05, unpaired student's t-tests.

982 **(K)** The cumulative fractions of mIPSC frequency were measured in control (black) and
983 cKO(red) PVH^{BDNF} neurons. The average frequency of events from a 2-minute stable recording
984 of each neuron is shown in the inset, unpaired student's t-tests.

985 **(L)** The cumulative fractions of mIPSC amplitude of control (black) and cKO (red) PVH^{BDNF}
986 neurons. The average amplitude of events from a 2-min stable recording of each neuron is
987 normalized to its capacitance and shown in the inset, unpaired student's t-tests.

988 **(M)** The area under the curve of each mIPSC event from a 2-minute recording is averaged.
989 Controls are shown in black, and cKOs are shown in red. unpaired t-tests, two-tailed. *p<0.05.

990 Data are shown as mean±SEM. Statistics: neuron numbers are in brackets (more than 3
991 mice/genotype)

992

993 **Figure 4: Selective *Rai1* ablation in PVH^{BDNF} neurons induces obesity**

994 **(A)** A schematic showing stereotaxic injection of adeno-associated viruses (AAVs) expressing
995 Cas9 protein and single-guide RNAs targeting *Rai1* (sgRai1) to delete *Rai1* from the PVH^{BDNF}
996 neurons of *Bdnf*$^{Cre/+}$ female mice. Scale bar = 50µm.

997 **(B)** Representative images showing that RAI1 immunoreactivity (cyan) was dramatically
998 reduced in *Bdnf*$^{Cre/+}$*; Ai9* mice injected with both sgRai1 and DIO-saCas9 viruses (Exp group n
999 =3, bottom row) into the PVH. In contrast, many PVH^{BDNF} neurons in *Bdnf*$^{Cre/+}$*; Ai9* mice
1000 injected only with the sgRai1 virus showed RAI1 expression (Ctrl group n =3, top row).

1001 **(C)** The percentage of PVH^{BDNF} neurons co-expressing RAI1 and GFP (virus) was significantly
1002 reduced in the Exp group, indicating a successful *Rai1* deletion. unpaired t-test, two-tailed,
1003 ****p<0.0001

1004 **(D)** PVH^{BDNF} neuron-specific *Rai1* deletion induced body weight gain in Exp mice (Ctrl group:
1005 n=5, Exp group: n =5). Two-way ANOVA with Šidák's multiple comparisons test. *p<0.05,
1006 **p < 0.01, ****p < 0.0001.

1007 **(E)** Body composition was measured with Echo-MRI, showing an increased fat mass deposition
1008 in 26-week-old Exp mice. ns indicates the difference is not significant. Two-way ANOVA with
1009 Šidák's multiple comparisons test. ***p<0.001, ****p < 0.0001.

1010 **(F)** Fat deposition analysis shows that the Exp group has significantly more subcutaneous
1011 inguinal (S.C.ing) and epididymal white adipose tissue (eWAT) mass (grams). ns indicates the
1012 difference is not significant. Two-way ANOVA with Šidák's multiple comparisons test. *p<0.05,
1013 ****p < 0.0001.

1014 **(G)** Representative images showing eWAT adipocyte hypertrophy of the Exp group (left). Scale
1015 bar = 500µm. Frequency distribution of adipocytes at each cellular size (right). ns indicates not
1016 significantly different. Two-way ANOVA with Šidák's multiple comparisons test. *$p<0.05$,
1017 ***$p<0.001$.

1018 **(H)** Exp and control mice showed similar food intake. ns indicates not significantly different,
1019 unpaired t-test, two-tailed.

1020 **(I)** Blood leptin levels were significantly increased in the Exp mice. unpaired t-test, two-tailed,
1021 *$p<0.05$.

1022 **(J)** Exp and control mice showed similar energy expenditure. ns indicates the difference is not
1023 significant. Two-way ANOVA with Šidák's multiple comparisons test.

1024 **(K)** Exp mice showed reduced locomotor activity in the dark phase. ns indicates the difference is
1025 not significant. Two-way ANOVA with Šidák's multiple comparisons test. *$p<0.05$.

1026 **(L)** Exp mice became hyperglycemic during the glucose tolerance test. ns indicates the
1027 difference is not significant. Two-way ANOVA with Šidák's multiple comparisons test. *$p<0.05$.

1028 **(M)** Measurement of the area under the curve (AUC) in Exp and Ctrl mice during the glucose
1029 tolerance test. unpaired t-test, two-tailed, $p=0.05$.

1030 **(N)** Exp mice showed increased plasma insulin levels during the glucose tolerance test. Two-way
1031 ANOVA with Šidák's multiple comparisons test, **$p<0.01$.

1032 Data are shown as mean±SEM.

1033

1034 **Figure 5: LM22A-4 treatment partially alleviates obesity and stereotypic behaviour in**
1035 **adult SMS mice**

1036 **(A)** Representative western blot showing p-AKT, total AKT, Histone 3 (H3, a loading control)
1037 levels in the hypothalamus of saline-treated Ctrl, saline-treated SMS and LM22A-4-treated SMS
1038 mice.

1039 **(B)** Quantification showing deficits in p-AKT levels of the hypothalamus were reversed by
1040 LM22A-4 treatment in SMS mice. Unpaired t-test, two-tailed, *$p<0.05$.

1041 **(C-E)** Body weight of saline-injected control, saline-injected SMS, and LM22A-4 injected SMS
1042 mice. Saline or LM22A-4 treatment periods were highlighted in orange. ns indicates not
1043 significantly different. Two-way ANOVA with Šidák's multiple comparisons test. *$p<0.05$,
1044 **$p < 0.01$, ****$p < 0.0001$.

1045 **(F)** Food intake (in grams) of saline-injected control, saline-injected SMS, and LM22A-4
1046 injected SMS mice. ns indicates the difference is not significant. unpaired t-test, two-tailed,
1047 *$p<0.05$, **$p < 0.01$.

1048 **(G)** Locomotor activity (number of beam breaks) for saline-injected control, saline-injected
1049 SMS, and LM22A-4 injected SMS mice. ns indicates the difference is not significant. unpaired t-
1050 test, two-tailed, *$p<0.05$.

1051 **(H)** Fat deposition analysis shows that the saline-injected SMS group has significantly more
1052 subcutaneous inguinal (S.C.ing) and epididymal white adipose tissue (eWAT) mass (grams) than
1053 saline-injected Ctrl mice. S.C.ing and eWAT mass in LM22A-4 injected mice is comparable to
1054 the saline-injected mice. Two-way ANOVA with Šidák's multiple comparisons test. **$p < 0.01$,
1055 ***$p<0.001$, ****$p < 0.0001$.

1056 **(I)** High-density lipoprotein (HDL) levels were restored to normal in LM22A-4 injected SMS
1057 mice. ns indicates the difference is not significant. unpaired t-test, two-tailed, **$p < 0.01$,
1058 ***$p<0.001$.

1059 **(J)** Insulin levels in saline-injected control, saline-injected SMS, and LM22A-4 injected SMS
1060 mice right before the start of the insulin tolerance test (time point 0). ns indicates the difference
1061 is not significant. unpaired t-test, two-tailed, *$p<0.05$.

1062 **(K)** Insulin tolerance test performed on saline-injected control, saline-injected SMS, and
1063 LM22A-4 injected SMS mice, two weeks post daily administration of LM22A-4 or saline, shows
1064 reductions in the blood glucose levels of LM22A-4 treated SMS mice. * Shows significance
1065 between saline-injected Ctrl and saline-injected SMS group. ns indicates the difference is not
1066 significant. Two-way ANOVA with Šidák's multiple comparisons test. **$p < 0.01$.

1067 **(L)** Stereotypic rearing behaviour was fully rescued in LM22A-4 treated SMS mice. ns indicates
1068 the difference is not significant. unpaired t-test, two-tailed. *$p<0.05$, **$p < 0.01$.

1069 Data are shown as mean±SEM.

1070

1071

1072

1073

1074

1075 **Fig 1-figure supplement 1: Differentially expressed proteins in the hypothalamus of SMS**
1076 **mice**

1077 A heat map showing hierarchical clustering of differentially expressed proteins in the
1078 hypothalamus of SMS mice.

1079

1080

1081 **Fig 2-figure supplement 1: The *Bdnf*^{Cre} allele labels BDNF-producing neurons in the**
1082 **paraventricular nucleus of the hypothalamus**

1083 **(A)** Schematic showing a transgenic mouse expressing *Bdnf*^{Cre}-dependent td-Tomato (Ai9)
1084 signals in BDNF-expressing cells.

1085 **(B-E)** Colocalization of *Bdnf*^{Cre}-dependent td-Tomato signals with endogenous BDNF protein.
1086 Black: DAPI, Magenta: BDNF-producing cells; Green: endogenous BDNF. Scale bar: 50 µm,
1087 yellow arrowheads indicate Ai9 marked BDNF cells coexpressing endogenous BDNF.

1088

1089

1090 **Fig 2-figure supplement 2: RAI1 expression in BDNF-expressing but not oxytocin-**
1091 **expressing magnocellular PVH neurons**

1092 **(A-H)** Representative images of DAPI expression (blue, **A**), oxytocin (green, **B**), BDNF-
1093 producing cells (Ai9 reporter, magenta, **C**), and RAI1 protein (cyan, **D**) in the PVH. Note that
1094 BDNF-producing neurons are distinct from the oxytocin-expressing neurons (**E**) and that RAI1 is
1095 more selectively expressed in the BDNF-expressing neurons (**F-H**).

1096 **(I)** Quantification showing the percentage of RAI1^{+} cells that co-express either BDNF (left bar,
1097 magenta) or oxytocin (right bar, green) in the PVH. n=3 mice/group. Data are shown as
1098 mean±SEM.

1099

1100

1101 **Fig 2-figure supplement 3: Ablating *Rai1* from the BDNF-producing cells induces body**
1102 **weight gain and defective energy homeostasis**

1103 **(A)** Schematic representation of the conditional knockout mice carrying either normal *Rai1*
1104 alleles and the Ai9 reporter in BDNF-producing cells (top) or homozygous *Rai1* deletion and the
1105 Ai9 reporter in the BDNF-producing cells.

1106 **(B)** Representative images showing the expression of DAPI (white), RAI1-expressing cells
1107 (green), and BDNF-expressing cells (Ai9 reporter, magenta) in the PVH. The top panel shows
1108 the Ctrl group with RAI1-Ai9 co-expression (yellow arrowheads) and the bottom panel shows
1109 reduced RAI1 and Ai9 colocalization (yellow arrowheads). Note that RAI1 expression was still
1110 detected in non-BDNF neurons in the PVH.

1111 **(C)** Quantification showing the percentage of BDNF-producing cells was not altered by *Rai1*
1112 deletion, indicating that RAI1 loss did not impair the generation or survival of PVH^{BDNF} neurons.
1113 ns indicates not significantly different, unpaired t-test, two-tailed.

1114 **(D)** The $Bdnf^{Cre/+}$ and $Bdnf^{Cre/+}$; $Rai1^{fl/+}$ female mice had similar body weights. ns indicates not
1115 significantly different. Two-way ANOVA with Šidák's multiple comparisons test.

1116 **(E-G)** Blood parameter analysis of triglycerides (TG), high-density lipoprotein (HDL), low-
1117 density lipoprotein and very low-density lipoprotein (LDL+VLDL) did not differ between Ctrl
1118 and cKO mice. ns indicates not significantly different, unpaired t-test, two-tailed.

1119 **(H)** The respiratory exchange rate did not differ between Ctrl and cKO mice. ns indicates the
1120 difference is not significant. Two-way ANOVA with Šidák's multiple comparisons test.

1121 **(I)** In the glucose tolerance test, the cKO mice showed an increased area under the curve (AUC).
1122 ***$p<0.001$, unpaired t-test, two-tailed.

1123 **(J)** In the glucose tolerance test, cKO mice showed increased insulin levels at the beginning of
1124 the test and 30 minutes after glucose administration. ns indicates the difference is not significant.
1125 Two-way ANOVA with Šidák's multiple comparisons tests, *$p < 0.05$, **$p<0.01$.

1126

1127 **(K)** In the insulin tolerance test, blood glucose level is measured after insulin injection. ns
1128 indicates the difference is not significant. Two-way ANOVA with Šidák's multiple comparisons
1129 test, *p < 0.05.

1130 Data are shown as mean±SEM.

1131

1132

1133

1134 **Fig 2-figure supplement 4: Metabolic profiles of male cKO mice lacking RAI1 expression in**
1135 **the BDNF-producing cells**

1136 **(A)** Male cKO mice gained significantly more weight than Ctrl mice beginning at 15 weeks of
1137 age. Two-way ANOVA with Šidák's multiple comparisons test, *p < 0.05, **p<0.01,
1138 ****p < 0.0001.

1139 **(B)** Male *Bdnf*$^{Cre/+}$ and *Bdnf*$^{Cre/+}$; *Rai1*$^{fl/+}$ mice had similar body weights. ns indicates the
1140 difference is not significant. Two-way ANOVA with Šidák's multiple comparisons test.

1141 **(C)** Echo-MRI analysis showed that 26-week-old male cKO mice had a significantly increased
1142 body weight due to increased fat but not lean mass. ns indicates the difference is not significant.
1143 unpaired t-test, two-tailed, **p<0.01, ****p<0.0001.

1144 **(D)** Fat disposition analysis showing the weight of brown adipocytes (BAT), subcutaneous
1145 inguinal (S.C.ing), and epididymal white adipose tissues (eWAT). ns indicates the difference is
1146 not significant. unpaired t-test, two-tailed, *p<0.05, **p<0.01.

1147 **(E)** Male cKO mice showed eWAT cell hypertrophy. Top: Representative images of the eWAT
1148 tissues in Ctrl and cKO mice. Scale bar = 500μm. Bottom: Frequency distribution of cellular
1149 sizes. Two-way ANOVA with Šidák's multiple comparisons test, *p < 0.05, **p<0.01,
1150 ***p<0.001, ****p < 0.0001.

1151 **(F-I)** Blood parameter analysis showing that male cKO mice showed significantly increased
1152 leptin levels **(F)** without alterations in TG **(G)**, HDL **(H)**, and LDL+VLDL **(I)**. ns indicates the
1153 difference is not significant. unpaired t-test, two-tailed. *p< 0.05.

1154 **(J)** No differences were found in the respiratory exchange rate in male Ctrl and cKO mice. ns
1155 indicates the difference is not significant. Two-way ANOVA with Šidák's multiple comparisons
1156 test.

1157 **(K)** Male cKO mice showed a significantly increased food intake compared to Ctrl littermates.,
1158 unpaired t-test, two-tailed, *p< 0.05.

1159 **(L)** Male cKO mice showed increased energy expenditure at the dark phase. ns indicates the
1160 difference is not significant. Two-way ANOVA with Šidák's multiple comparisons test, *p<0.05.

1161 **(M)** Male Ctrl and cKO mice showed similar locomotor activities. ns indicates the difference is
1162 not significant. Two-way ANOVA with Šidák's multiple comparisons test.

1163 **(N-P)** Glucose tolerance test shows that cKO male mice are glycemic 45 minutes post
1164 intraperitoneal glucose administration **(N)** and had increased AUC (unpaired t-test, two-tailed)
1165 **(O)**, despite significantly higher insulin levels before and 30 minutes after glucose administration
1166 **(P)**, suggesting potential insulin insensitivity. ns indicates the difference is not significant. Two-
1167 way ANOVA with Šidák's multiple comparisons tests, *p<0.05, **p < 0.01, ***p<0.001.

1168 **(Q)** Insulin tolerance test showing that male cKO mice showed significantly higher blood
1169 glucose levels 60 minutes after intraperitoneal insulin administration. Two-way ANOVA with
1170 Šidák's multiple comparisons test, *p<0.05, **p < 0.01.

1171 Data are shown as mean±SEM.

1172

1173 **Fig 3-figure supplement 1: The cellular and synaptic properties of control and *Rai1*-**
1174 **deficient PVH^{BDNF} neurons**

1175 **(A)** Representative traces of rebound and rebound repetitive firing of PVH^{BDNF} neurons in
1176 control (black) and cKO (red).

1177 **(B)** Representative AP waveforms at holding voltages of -80mV, -60mV, and -50mV in control
1178 (left) and -50mV and -45mV in cKO (right).

1179 **(C)** The half-width of AP initiated at a holding voltage of -60mV (neuronal numbers in brackets,
1180 ns indicates the difference is not significant, unpaired t-test, two-tailed).

1181 **(D)** Representative traces of miniature recordings in control (black) and cKO (red) PVH^{BDNF}
1182 neurons. The traces were recorded with a Cs-based internal at a holding voltage of -70mV in
1183 aCSF (top), spontaneous mEPSCs were recorded in aCSF containing 1uM TTX at a holding
1184 voltage of -70mV (middle), and mIPSCs were recorded at holding voltage of +10mV (bottom).

1185 **(E)** Quantification showing that the cellular size of cKO PVH^{BDNF} neurons was significantly
1186 smaller than Ctrl neurons. unpaired t-test, two-tailed. ****$p<0.0001$.

1187

1188

1189 **Fig 4-figure supplement 1: Metabolic profile of mice lacking *Rai1* in PVH^{BDNF} neurons**

1190 **(A)** Representative images showing co-expression of virus-infected cells (GFP/green), *Bdnf*^{Cre}-
1191 dependent Ai9 signals (BDNF cells, magenta), and endogenous RAI1 (cyan). Yellow arrowheads
1192 indicate BDNF neurons infected with AAV and in these cells, RAI1 signals were diminished in
1193 Exp but not Ctrl mice. Scale bar = 50µm.

1194 **(B-C)** The total number of PVH^{BDNF} neurons **(B)** and total number of PVH^{BDNF} neurons infected
1195 with AAVs **(C)** per slice show that *Rai1* deletion or virus infection did not alter the total number
1196 of PVH^{BDNF} neurons. ns indicates the difference is not significant. unpaired t-test, two-tailed.

1197 **(D)** *Rai1* expression was significantly reduced in PVH^{BDNF} neurons infected with both AAVs
1198 compared to PVH^{BDNF} neurons infected with sgRai1-GFP AAV alone. unpaired t-test, two-tailed,
1199 **$p<0.01$.

1200 **(E)** The number of PVH^{BDNF} neurons that co-express RAI1 was significantly reduced in the Exp
1201 group. unpaired t-test, unpaired, **$p<0.01$.

1202 **(F)** Representative image showing lack of viral expression in the PVH neighbouring nuclei.
1203 ARC: arcuate nucleus. VMH: ventromedial nucleus of the hypothalamus. 3V: third ventricle.
1204 Scale bar = 50µm.

1205 (**G**) The respiratory exchange rate remained similar in Ctrl and Exp mice. ns indicates the
1206 difference is not significant. Two-way ANOVA, Šídák's multiple comparisons test.

1207 **(H-J)** Blood parameter analysis showing TG, HDL, and LDL+VLDL levels were similar in Ctrl
1208 and Exp mice. ns indicates the difference is not significant. unpaired t-test, two-tailed.

1209 **(K)** In the insulin tolerance test, the Exp group showed a trend towards increased blood glucose
1210 levels after insulin injection. Two-way ANOVA, Šídák's multiple comparisons test.

1211 Data are shown as mean±SEM.

1212

1213

1214 **Figure 5—figure supplement 1: LM22A-4 treatment does not disrupt energy homeostasis**
1215 **and repetitive rearing in the Ctrl mice**

1216 **(A)** LM22A-4 concentration in the hypothalamus and forebrain of SMS mice 1 hour (black dots)
1217 and 3 hours (red dots) after simultaneous intranasal and IP injections.

1218 **(B)** Four independent sets of western blotting analyses showing reduced p-AKT levels in the
1219 hypothalamus of saline-treated SMS mice, which were increased by LM22A-4 treatment. Total
1220 AKT protein was used as a control.

1221 **(C)** Similar body weight of Ctrl mice treated with either saline or LM22A-4. ns indicates the
1222 difference is not significant. Two-way ANOVA, Šídák's multiple comparisons test.

1223 **(D)** Energy expenditure was not different between groups in the light vs. dark phase. ns indicates
1224 the difference is not significant. Two-way ANOVA, Šídák's multiple comparisons test.

1225 **(E)** Respiratory exchange rates were not different between groups in the light vs. dark phase. ns
1226 indicates the difference is not significant. Two-way ANOVA, Šídák's multiple comparisons test.

1227 **(F)** Repetitive rearing behaviour in Ctrl mice was not altered by LM22A-4 treatment. ns
1228 indicates the difference is not significant. unpaired t-test, two-tailed.

1229 Data are shown as mean±SEM.

1230

1231

1232 **Figure 5—figure supplement 2: LM22A-4 treatment in adult SMS mice is insufficient to**
1233 **improve social interaction deficit**

1234 **(A)** Schematic showing the tube test that assesses social interaction between stranger mice of
1235 different genotypes.

1236 **(B)** 7-week-old Ctrl mice won significantly more than SMS mice before the LM22A-4 treatment.
1237 unpaired t-test, two-tailed. ****$p<0.0001$.

1238 **(C)** 10-week-old saline-injected Ctrl mice won significantly more than the saline-injected SMS
1239 mice (two weeks post-LM22A-4 treatment). unpaired t-test, two-tailed, ***$p<0.001$.

1240 **(D)** 10-week-old saline-injected Ctrl mice won significantly more than LM22A-4 injected SMS
1241 mice. unpaired t-test, two-tailed, *$p<0.05$.

1242 **(E)** 10-week-old saline-injected SMS mice showed a similar winning rate to LM22A-4-injected
1243 SMS mice. ns indicates the difference is not significant. unpaired t-test, two-tailed.

1244 Data are shown as mean±SEM.

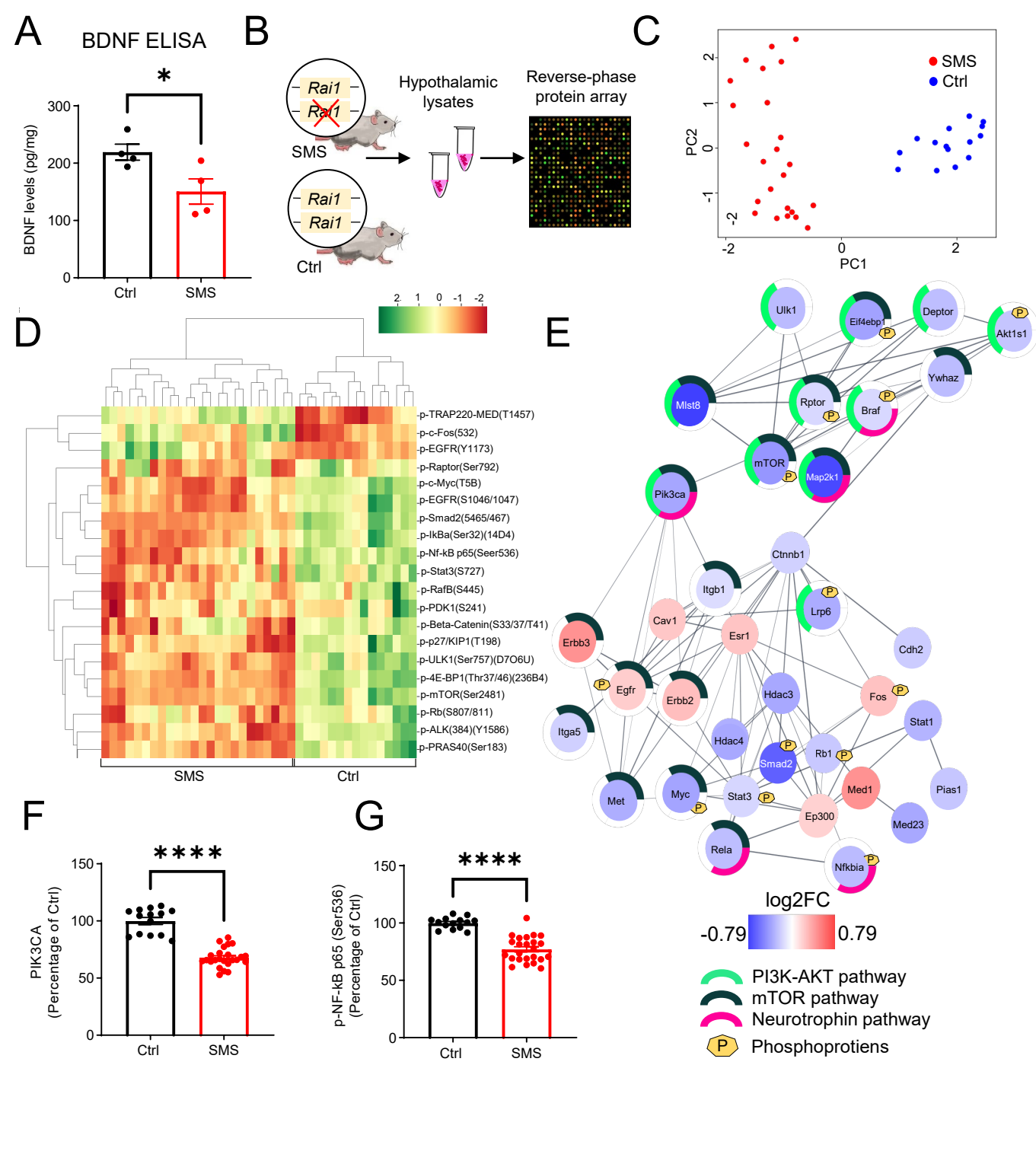
A
BDNF ELISA
*
BDNF levels (pg/mg)
300
200
100
0
Ctrl
SMS
B
Rai1
Rai1
SMS
Rai1
Rai1
Ctrl
Hypothalamic lysates
Reverse-phase protein array
C
SMS
Ctrl
PC2
PC1
2
1
0
-1
-2
D
2
1
0
-1
-2
p-TRAP220-MED(T1457)
p-c-Fos(532)
p-EGFR(Y1173)
p-Raptor(Ser792)
p-c-Myc(T5B)
p-EGFR(S1046/1047)
p-Smad2(5465/467)
p-IkBa(Ser32)(14D4)
p-Nf-kB p65(Seer536)
p-Stat3(S727)
p-RafB(S445)
p-PDK1(S241)
p-Beta-Catenin(S33/37/T41)
p-p27/KIP1(T198)
p-ULK1(Ser757)(D7O6U)
p-4E-BP1(Thr37/46)(236B4)
p-mTOR(Ser2481)
p-Rb(S807/811)
p-ALK(384)(Y1586)
p-PRAS40(Ser183)
SMS
Ctrl
E
Ulk1
Eif4ebp1
Deptor
Akt1s1
Ywhaz
Mlst8
Rptor
Braf
mTOR
Map2k1
Pik3ca
Ctnnb1
Itgb1
Lrp6
Cav1
Esr1
Erbb3
Cdh2
Egfr
Erbb2
Hdac3
Fos
Stat1
Itga5
Hdac4
Smad2
Rb1
Med1
Pias1
Met
Myc
Stat3
Ep300
Med23
Rela
Nfkbia
P
log2FC
-0.79
0.79
PI3K-AKT pathway
mTOR pathway
Neurotrophin pathway
Phosphoprotiens
F
****
PIK3CA (Percentage of Ctrl)
150
100
50
0
Ctrl
SMS
G
****
p-NF-kB p65 (Ser536) (Percentage of Ctrl)
150
100
50
0
Ctrl
SMS

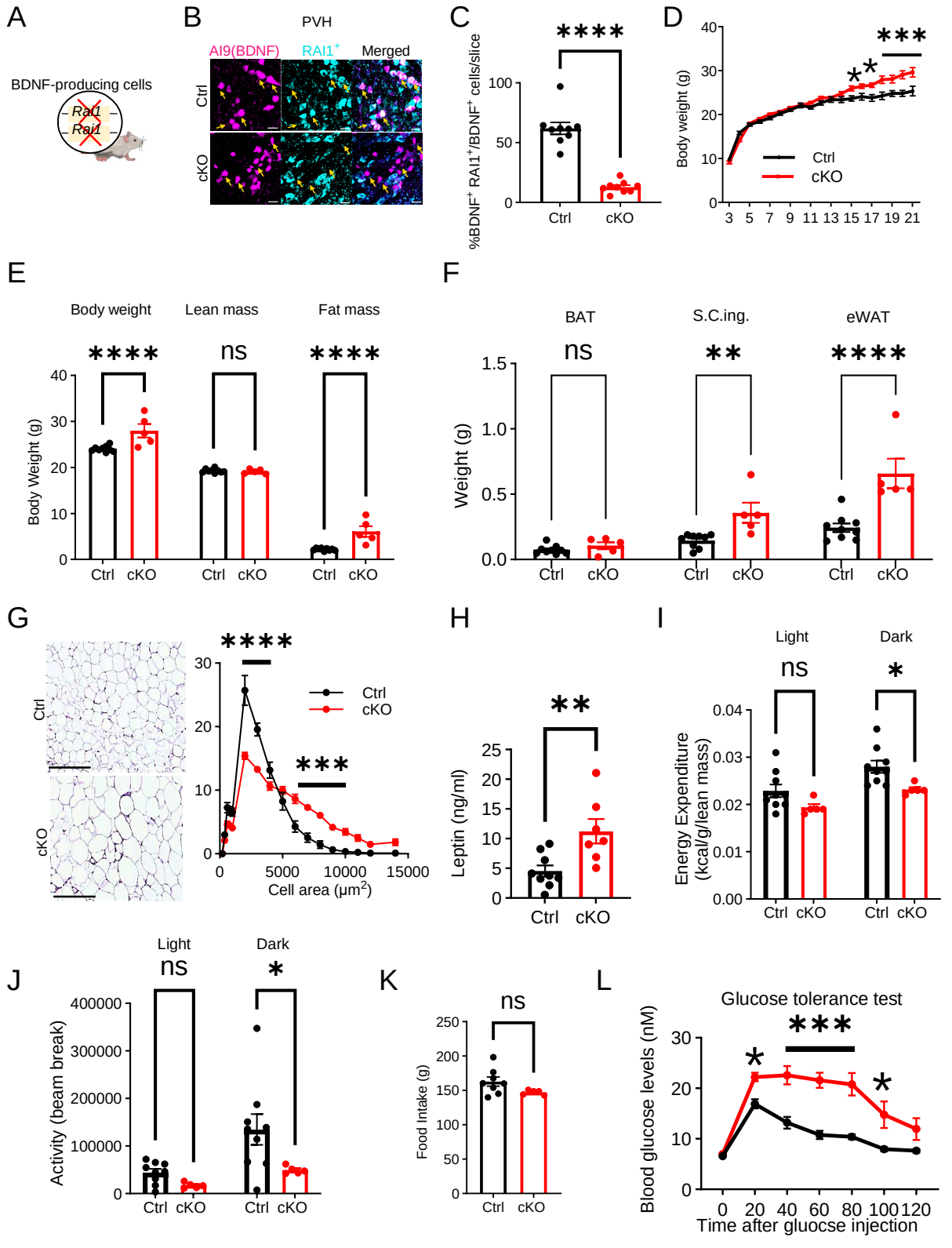
A
BDNF-producing cells
Ral1
Ral1
B
PVH
AI9(BDNF)
RAI1+
Merged
Ctrl
cKO
C
****
%BDNF+ RAI1+/BDNF+ cells/slice
100
50
0
Ctrl
cKO
D
***
**
Body weight (g)
40
30
20
10
0
Ctrl
cKO
3 5 7 9 11 13 15 17 19 21
E
Body weight
Lean mass
Fat mass
****
ns
****
Body Weight (g)
40
30
20
10
0
Ctrl cKO Ctrl cKO Ctrl cKO
F
BAT
S.C.ing.
eWAT
ns
**
****
Weight (g)
1.5
1.0
0.5
0.0
Ctrl cKO Ctrl cKO Ctrl cKO
G
Ctrl
cKO
****
***
Ctrl
cKO
30
20
10
0
0 5000 10000 15000
Cell area (μm2)
H
**
Leptin (ng/ml)
25
20
15
10
5
0
Ctrl cKO
I
Light
Dark
ns
*
Energy Expenditure (kcal/g/lean mass)
0.04
0.03
0.02
0.01
0.00
Ctrl cKO Ctrl cKO
J
Light
Dark
ns
*
Activity (beam break)
400000
300000
200000
100000
0
Ctrl cKO Ctrl cKO
K
ns
Food Intake (g)
250
200
150
100
50
0
Ctrl cKO
L
Glucose tolerance test
***
*
*
Blood glucose levels (nM)
30
20
10
0
0 20 40 60 80 100 120
Time after gluocse injection

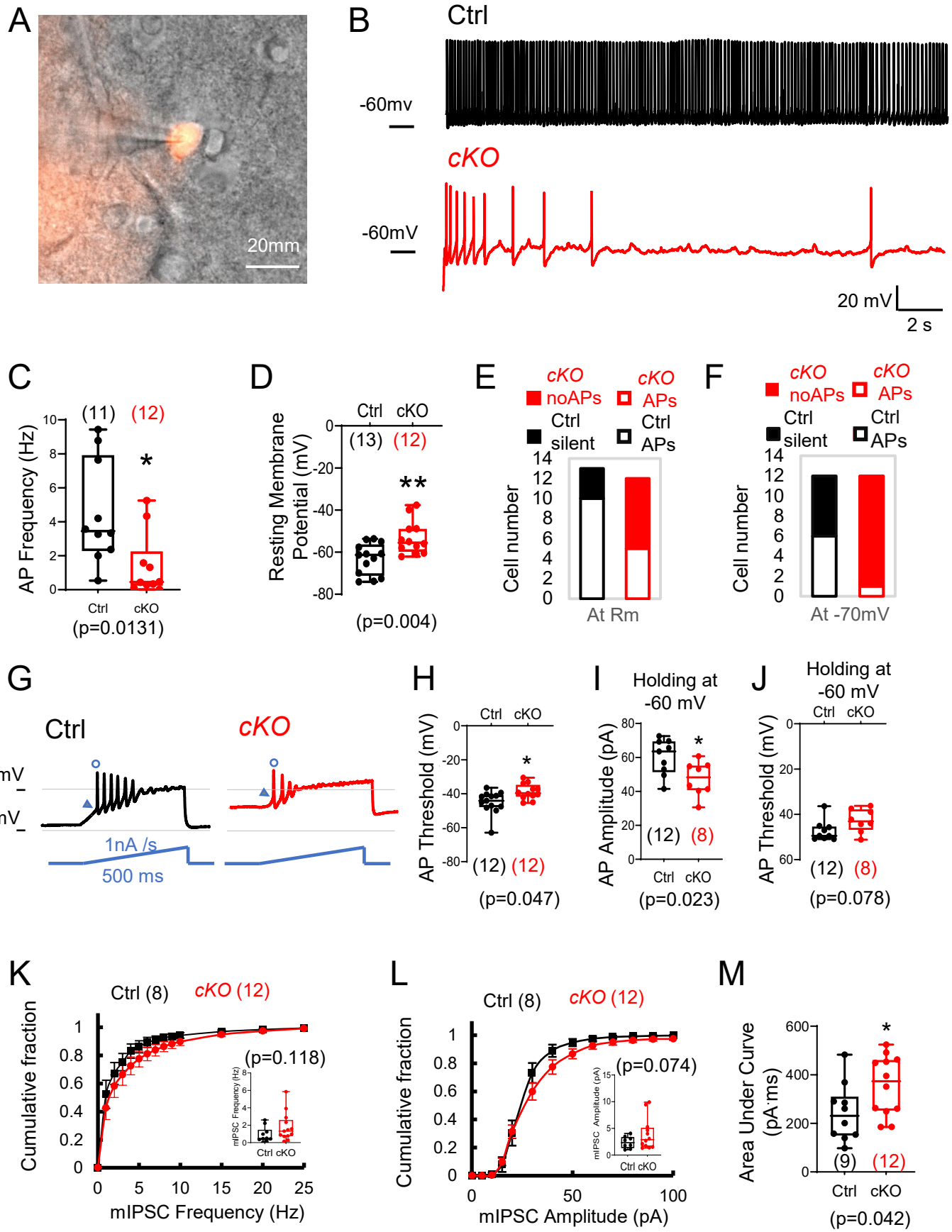
A
20mm
B
Ctrl
-60mv
cKO
-60mV
20 mV
2 s
C
AP Frequency (Hz)
(11)
(12)
*
Ctrl
cKO
(p=0.0131)
D
Resting Membrane Potential (mV)
Ctrl
cKO
(13)
(12)
**
(p=0.004)
E
cKO noAPs
cKO APs
Ctrl silent
Ctrl APs
Cell number
At Rm
F
cKO noAPs
cKO APs
Ctrl silent
Ctrl APs
Cell number
At -70mV
G
Ctrl
cKO
-40mV
-60mV
1nA /s
500 ms
H
AP Threshold (mV)
Ctrl
cKO
*
(12)
(12)
(p=0.047)
I
Holding at -60 mV
AP Amplitude (pA)
*
(12)
(8)
Ctrl
cKO
(p=0.023)
J
Holding at -60 mV
AP Threshold (mV)
Ctrl
cKO
(12)
(8)
(p=0.078)
K
Ctrl (8)
cKO (12)
Cumulative fraction
(p=0.118)
mIPSC Frequency (Hz)
L
Ctrl (8)
cKO (12)
Cumulative fraction
(p=0.074)
mIPSC Amplitude (pA)
M
Area Under Curve (pA·ms)
*
(9)
(12)
Ctrl
cKO
(p=0.042)

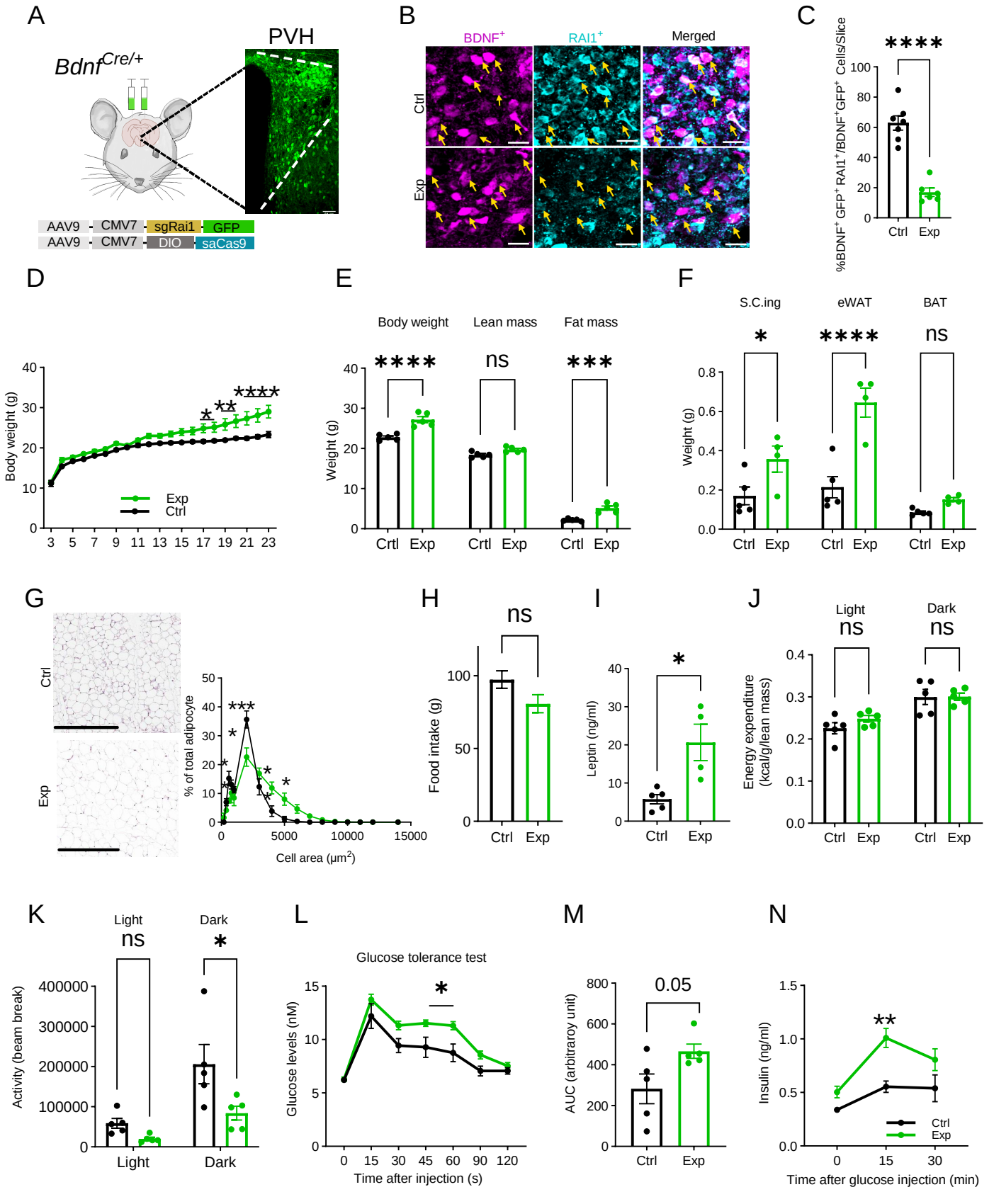
A
Bdnf Cre/+
PVH
AAV9 - CMV7 - sgRai1 - GFP
AAV9 - CMV7 - DIO - saCas9
B
BDNF+
RAI1+
Merged
Ctrl
Exp
C
%BDNF+ GFP+ RAI1+/BDNF+GFP+ Cells/Slice
****
Ctrl
Exp
D
Body weight (g)
Exp
Ctrl
E
Body weight
Lean mass
Fat mass
Weight (g)
****
ns
***
Crtl
Exp
F
S.C.ing
eWAT
BAT
Weight (g)
*
****
ns
Ctrl
Exp
G
Ctrl
Exp
% of total adipocyte
Cell area (μm2)
H
ns
Food intake (g)
I
*
Leptin (ng/ml)
J
Light
Dark
ns
ns
Energy expenditure (kcal/g/lean mass)
K
Light
Dark
ns
*
Activity (beam break)
L
Glucose tolerance test
*
Glucose levels (nM)
Time after injection (s)
M
0.05
AUC (arbitraroy unit)
N
**
Insulin (ng/ml)
Ctrl
Exp
Time after glucose injection (min)

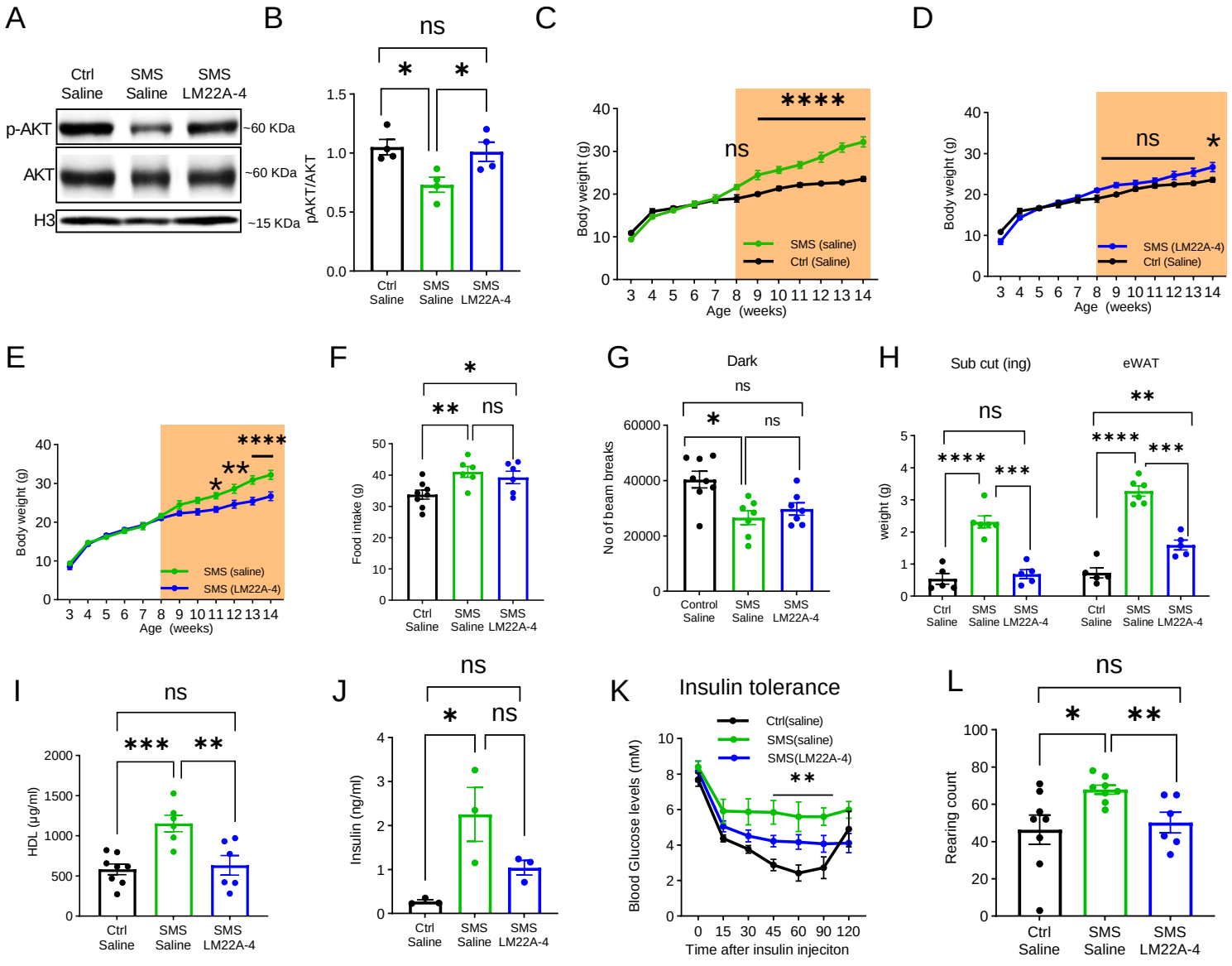
A
Ctrl Saline
SMS Saline
SMS LM22A-4
p-AKT
AKT
H3
~60 KDa
~60 KDa
~15 KDa
B
ns
*
*
pAKT/AKT
1.5
1.0
0.5
0.0
Ctrl Saline
SMS Saline
SMS LM22A-4
C
****
ns
Body weight (g)
SMS (saline)
Ctrl (Saline)
Age (weeks)
D
ns
*
Body weight (g)
SMS (LM22A-4)
Ctrl (Saline)
Age (weeks)
E
****
**
*
Body weight (g)
SMS (saline)
SMS (LM22A-4)
Age (weeks)
F
*
**
ns
Food intake (g)
Ctrl Saline
SMS Saline
SMS LM22A-4
G
Dark
ns
*
ns
No of beam breaks
Control Saline
SMS Saline
SMS LM22A-4
H
Sub cut (ing)
eWAT
ns
****
***
**
****
***
weight (g)
Ctrl Saline
SMS Saline
SMS LM22A-4
I
ns
***
**
HDL (μg/ml)
Ctrl Saline
SMS Saline
SMS LM22A-4
J
ns
*
ns
Insulin (ng/ml)
Ctrl Saline
SMS Saline
SMS LM22A-4
K
Insulin tolerance
Ctrl(saline)
SMS(saline)
SMS(LM22A-4)
**
Blood Glucose levels (mM)
Time after insulin injeciton
L
ns
*
**
Rearing count
Ctrl Saline
SMS Saline
SMS LM22A-4